



A resolvent-based prediction framework for incompressible turbulent channel flow with limited measurements

Anjia Ying¹, Tian Liang¹, Zhigang Li¹ and Lin Fu^{1,2,3,4,†}

¹Department of Mechanical and Aerospace Engineering, The Hong Kong University of Science and Technology, Clear Water Bay, Kowloon, Hong Kong

²Department of Mathematics, The Hong Kong University of Science and Technology, Clear Water Bay, Kowloon, Hong Kong

³HKUST Shenzhen-Hong Kong Collaborative Innovation Research Institute, Futian, Shenzhen, PR China

⁴Center for Ocean Research in Hong Kong and Macau (CORE), The Hong Kong University of Science and Technology, Clear Water Bay, Kowloon, Hong Kong

(Received 31 May 2023; revised 8 September 2023; accepted 11 October 2023)

A new resolvent-based method is developed to predict the space–time properties of the flow field. To overcome the deterioration of the prediction accuracy with increasing distance between the measurements and predictions in the resolvent-based estimation (RBE), the newly proposed method utilizes the RBE to estimate the relative energy distribution near the wall rather than the absolute energy directly estimated from the measurements. Using this extra information from RBE, the new method modifies the energy distribution of the spatially uniform and uncorrelated forcing that drives the flow system by minimizing the norm of the cross-spectral density tensor of the error matrix in the near-wall region in comparison with the RBE-estimated one, and therefore it is named as the resolvent-informed white-noise-based estimation (RWE) method. For validation, three time-resolved direct numerical simulation (DNS) datasets with the friction Reynolds numbers $Re_\tau = 180, 550$ and 950 are generated, with various locations of measurements ranging from the near-wall region ($y^+ = 40$) to the upper bound of the logarithmic region ($y/h \approx 0.2$, where h is the half-channel height) for the predictions. Besides the RWE, three existing methods, i.e. the RBE, the λ -model and the white-noise-based estimation (WBE), are also included for the validation. The performance of the RBE and scale-dependent model (λ -model) in predicting the energy spectra shows a strong dependence on the measurement locations. The newly proposed RWE shows a low sensitivity on Re_τ and the measurement locations, which may range from the near-wall region to the upper bound of the logarithmic region, and has a high accuracy in predicting the energy spectra. The RWE also performs well in predicting the space–time properties in terms of the correlation

† Email address for correspondence: linfu@ust.hk

magnitude and the convection velocity. We further utilize the new method to reconstruct the instantaneous large-scale structures with measurements from the logarithmic region. Both the RWE and RBE perform well in estimating the instantaneous large-scale structure, and the RWE has smaller errors in the estimations near the wall. The structural inclination angles around 15° are predicted by the RWE and WBE, which generally recover the DNS results.

Key words: boundary layer structure, turbulence modelling, turbulent boundary layers

1. Introduction

Credible predictions of turbulent flows have long been an essential concern for numerical and experimental studies. However, in many cases, only part of the flow information could be obtained due to the inaccuracy of the numerical models or the limitations of the experimental measurement techniques. For instance, in the numerical studies, the popular wall-modelled large-eddy simulation (WMLES) resolves only the large-scale flow motions beyond the local grid scale and models the effect of the near-wall small-scale motions with Reynolds-averaged Navier–Stokes (RANS)-like methods to balance the accuracy and cost for turbulence simulation; see e.g. Larsson *et al.* (2016), Fu *et al.* (2021) and Fu, Bose & Moin (2022). However, the velocity fluctuation in the near-wall region, which is an important turbulence property, is missing or inaccurate in WMLES (Bae *et al.* 2018). As for the experimental studies, the measuring points are usually sparsely placed in space due to technical limitations, and important flow information might be lost. To derive the missing flow information in the unresolved or unmeasured regions, many researchers attempt to estimate the turbulence statistics from limited sets of available flow data, the methodologies of which could be generally categorized into the data-driven approaches (Townsend 1976; Marusic, Mathis & Hutchins 2010; Baars, Hutchins & Marusic 2016; Guastoni *et al.* 2021) and the physics-based approaches (Hwang & Cossu 2010; McKeon & Sharma 2010).

The data-driven approaches predict the flow statistics based on the fundamental research on the statistical properties of wall-bounded turbulence, where the widely recognized attached eddy model (AEM) (Townsend 1976) and inner–outer interaction model (IOIM) (Marusic *et al.* 2010; Baars *et al.* 2016) are proposed and extensively validated. The AEM considers the turbulence properties in the logarithmic region to be characterized by a collection of self-similar energy-containing eddies whose roots are attached to the wall. From the basic concept of attached eddies, many kinds of statistics of turbulence could be derived, such as the logarithmic profile of the variance of the streamwise velocity fluctuations. From AEM, the logarithmic laws could be further extended to describe the wall-normal distributions of higher-order even moments (Meneveau & Marusic 2013; de Silva *et al.* 2015; Yang, Marusic & Meneveau 2016). On the other hand, the IOIM states that the near-wall turbulence is influenced by the large-scale motions and very-large-scale motions via the superposition and modulation effects, which also paves the way to predict the near-wall turbulence using the velocity data in the logarithmic region. Recently, the consistency between the AEM and the IOIM has been demonstrated by Cheng & Fu (2022), which enables isolating of the attached eddies at a given single scale and further predicting their separated superposition effect in the near-wall region. With the isolated attached eddies at a given length scale, the turbulence properties can be further clarified (Cheng, Shyy & Fu 2022; Cheng & Fu 2023). However, in practice, the IOIM needs the given data at the near-wall region to calculate the transfer kernel for predicting the footprint of the attached eddies in the near-wall region, which could not be directly applied for the

predictions when the second-order flow statistics are not available. Meanwhile, the AEM only considers the attached eddies that are dominant in the logarithmic region, which is not the case in the inner and buffer layers, where the smaller detached eddies are significant. Besides the above models describing the turbulence, the convolutional neural network (CNN) is also used for the data-driven prediction of the turbulence properties (Guastoni *et al.* 2021; Güemes *et al.* 2021). For instance, using the model parameters trained from the existing datasets, Guastoni *et al.* (2021) reconstruct the flow field with the shear stress measurements at the wall.

In addition to the data-driven approaches, the physics-based ones predict the turbulence field based on the Navier–Stokes equations, which govern the flow dynamics. In general, the physics-based approaches rearrange the Navier–Stokes equations to the form of the linearized relationship between the nonlinear forcing (input) and the response of velocity, pressure and temperature (output) (Hwang & Cossu 2010; McKeon & Sharma 2010). Specifically, when the linearized relationship is defined in the frequency domain, the operator that builds the linear relationship is named the resolvent operator (McKeon & Sharma 2010). Taking Fourier transformation to the linearized Navier–Stokes equations in all the uniform spatial and temporal directions, the linearized relationship between the nonlinear forcing and the response at each scale is extracted, where the nonlinear forcing involves the convolutions from all the other scales (McKeon 2017). So far, the relationship between the forcing and the response is equivalent to the original form of the Navier–Stokes equations without any assumptions. The response could be fully recovered as long as the nonlinear forcing is completely known (Morra *et al.* 2021). However, the completed knowledge of the nonlinear forcing is unavailable as long as the flow data are not totally known. Despite this point, important turbulent properties can be extracted from the resolvent operator itself when the mean velocity profile is known. For instance, the forcing and response modes ordered by their gains could be obtained after taking singular value decomposition to the resolvent operator. When the gain of the leading mode dominates those of the sequential modes, which is referred to as the low-rank behaviour (Pickering *et al.* 2021), it can effectively construct a low-dimensional description of the turbulence (Moarref *et al.* 2013; Sharma & McKeon 2013; McKeon 2017). Assuming the low-rank behaviour, Beneddine *et al.* (2016) predict the streamwise velocity spectra by fitting the amplitude of the leading response mode, which minimizes the square of the error between the predicted profile and the measurements at different positions. However, the energy of the leading resolvent mode is not always predominant over the following modes (Morra *et al.* 2021), which means that only taking the leading mode inevitably sacrifices much information.

Rather than considering only the leading mode, another group of physics-based approaches implicitly take advantage of the low-rank behaviour by treating the unknown nonlinear forcing as white in space (Hwang & Cossu 2010; Madhusudanan, Illingworth & Marusic 2019; Morra *et al.* 2019). Since the white-noise assumptions imply that the energies of nonlinear forcing modes are equal to each other among all the modes (Towne, Schmidt & Colonius 2018), the energies of the response modes are proportional to the gains accordingly. By modelling a part of the forcing with the eddy-viscosity terms (Cess 1958; Reynolds & Hussain 1972) in the linearized Navier–Stokes equations and assuming that the remaining forcing is white noise, the accuracy of prediction on the fluctuation statistics is much improved (Hwang & Cossu 2010; Morra *et al.* 2019). Later, Madhusudanan *et al.* (2019) estimate the superposition effect of the large-scale structures on the near-wall region using the eddy-viscosity model with the remaining forcing assumed as white noise. Gupta *et al.* (2021) further improve the work of Madhusudanan *et al.* (2019) by modifying the forcing profile according to the wall-normal distributions of the eddy viscosity and flow scales.

Besides the above approaches that assume a predefined forcing profile, the Kalman filter-based approaches (Høpfner *et al.* 2005; Chevalier *et al.* 2006) and resolvent-based approaches (Martini *et al.* 2020; Towne, Lozano-Durán & Yang 2020) are also proposed. Illingworth, Monty & Marusic (2018) estimate the large-scale structures in wall turbulence with the H_2 -optimal approaches. Illingworth *et al.* (2018) also demonstrate significant improvement in the predictions when the eddy-viscosity term is introduced in the linearized Navier–Stokes equations. Towne *et al.* (2020) predict the two-point space–time statistics in the near-wall region of turbulent channel flow by estimating the minimum forcing that could fully reproduce the measurements, namely the resolvent-based estimation (RBE). Since the approach only estimates the minimum forcing that recovers the observations, it underestimates the forcing that generates large responses at other positions but has minor effects on the measurements (Karban *et al.* 2022). In terms of practical applications, the measurements are not guaranteed to be located in the vicinity of the prediction region, which means that the direct applications of RBE are limited. Later, Martini *et al.* (2020) generalizes the RBE approach by taking the forcing colour and sensor noise into account when constructing the transfer function for estimation. An optimal linear estimator of the flow states can be obtained by taking the real forcing cross-spectral density (CSD) tensors as input. In practice, the forcing statistics can be estimated from additional sensors or approximated from reasonable models. The improved RBE (Martini *et al.* 2020) recovers the original one (Towne *et al.* 2020) when the forcing is assumed to be white in space and the sensor noise is neglected. Amaral *et al.* (2021) predict the turbulent channel flow with wall shear stress and pressure using the improved RBE, showing that the flow information can be better predicted when the actual forcing spectra are already known. In practice, a method that can avoid rather predefined or already-known forcing statistics is indeed needed to fill the gap between theory and real applications.

With the current physics-based methods, the predictions based on the white-noise assumptions (Madhusudanan *et al.* 2019; Morra *et al.* 2019; Gupta *et al.* 2021) could represent the general properties of the turbulence, but the accuracy is limited. On the other hand, without known forcing statistics, the RBE (Towne *et al.* 2020) performs well when the prediction layer is located near the measurement layer but becomes invalid when the prediction location moves far away from the measurement location. In cases where the measurements are not close to the prediction region, both the methods based on white-noise assumptions and the RBE are not expected to provide accurate predictions on the flow information. However, these two kinds of methods could compensate for each other in a sense. The new method proposed in this study builds the skeleton of forcing based on the white noise to maintain the predicted response energy even when the measurement is far away from the prediction, while refines the forcing profile with near-wall relative energy profile from the RBE results. Through the above procedure, the advantages of these two kinds of methods are combined in the new approach.

The remainder of this article is organized as follows. In § 2, existing prediction methods are reviewed and discussed. In § 3, the prediction method is derived and illustrated. In § 4, the newly proposed method is validated by comparing the prediction with the results from the direct numerical simulation (DNS) data and existing prediction methods. Discussions and concluding remarks are presented in § 5.

2. The existing methods

In this section, the mathematical description of the resolvent analysis is introduced, followed by a brief review of the existing methods to predict the flow field, including the white-noise-based estimation (WBE) (Morra *et al.* 2019), the wall-distance-dependent

model (W-model) and the scale-dependent model (λ -model) (Gupta *et al.* 2021), as well as the RBE (Martini *et al.* 2020; Towne *et al.* 2020). Basic ideas of the to-be-reviewed methods will form the cornerstone of our newly proposed method derived in § 3.

2.1. *Mathematical description of the resolvent analysis*

The incompressible Navier–Stokes equations are given by

$$\frac{\partial \mathbf{u}}{\partial t} + \mathbf{u} \cdot \nabla \mathbf{u} = -\nabla p + \frac{1}{Re_\tau} \nabla \cdot (\nabla \mathbf{u} + \nabla \mathbf{u}^T), \tag{2.1a}$$

$$\nabla \cdot \mathbf{u} = 0, \tag{2.1b}$$

where $Re_\tau = u_\tau h/\nu$ is the friction Reynolds number, u_τ is the friction velocity, h is the half-channel height, ν is the kinematic viscosity and the superscript T denotes transpose. Following the previous studies (Illingworth *et al.* 2018; Morra *et al.* 2019; Towne *et al.* 2020), the forcing \mathbf{f} that contains the nonlinear interactions of velocity fluctuations while excluding the eddy-viscosity term is defined as

$$\mathbf{f} = -\mathbf{u}' \cdot \nabla \mathbf{u}' - \frac{1}{Re_\tau} \nabla \cdot \left[\frac{\nu_t}{\nu} (\nabla \mathbf{u}' + \nabla \mathbf{u}'^T) \right], \tag{2.2}$$

where the superscript $'$ denotes the fluctuation variable. Here, the eddy viscosity ν_t is calculated from the semi-empirical expression by Cess (1958) and reported by Reynolds & Hussain (1972) as

$$\nu_t = \frac{\nu}{2} \left\{ 1 + \frac{\kappa^2 Re_\tau^2}{9} (2y - y^2)^2 (3 - 4y + 2y^2)^2 \left[1 - \exp\left(\frac{-Re_\tau y}{A}\right) \right]^2 \right\}^{1/2} - \frac{\nu}{2}, \tag{2.3}$$

where the constants $\kappa = 0.426$ and $A = 25.4$. By rearranging (2.1), the linearized Navier–Stokes equations hold

$$\frac{\partial \mathbf{u}'}{\partial t} + \bar{\mathbf{u}} \cdot \nabla \mathbf{u}' + \mathbf{u}' \cdot \nabla \bar{\mathbf{u}} + \nabla p' - \frac{1}{Re_\tau} \nabla \cdot \left[\frac{\nu_T}{\nu} (\nabla \mathbf{u}' + \nabla \mathbf{u}'^T) \right] = \mathbf{f}, \tag{2.4a}$$

$$\nabla \cdot \mathbf{u}' = 0, \tag{2.4b}$$

where $\bar{\mathbf{u}}$ is the mean velocity, and $\nu_T = \nu_t + \nu$ is the total viscosity. Note that (2.4a,b) are equivalent to the incompressible Navier–Stokes equations (2.1a,b).

From (2.2) and (2.4), the inclusion of the eddy viscosity model into the linearized Navier–Stokes equations changes both the definition of forcing and the linearized relationship between the forcing and response. In McKeon & Sharma (2010), the total forcing is defined as $\mathbf{f} = -\mathbf{u}' \cdot \nabla \mathbf{u}'$. The forcing re-defined in this study is equivalent to the remaining portion of the forcing in McKeon & Sharma (2010) after excluding the eddy-viscosity term $(1/Re_\tau) \nabla \cdot [\nu_T/\nu (\nabla \mathbf{u}' + \nabla \mathbf{u}'^T)]$. In the following sections, the tested prediction methods actually provide different approaches to model the re-defined forcing in (2.2). The total forcing, on the other hand, is equal to the summation of the portion that is modelled by the eddy-viscosity terms and the remaining portion that is modelled by the prediction methods.

The linearized Navier–Stokes equations in each spatial scale \mathbf{k}_s are obtained by taking the Fourier transformation to (2.4) in the uniform spatial directions. For instance, in the fully developed turbulent channel flow, the Fourier transformation is taken in the streamwise (x) and spanwise (z) directions. The linearized equations (2.4) at $\mathbf{k}_s = (k_x, k_z)$

can be therefore written in a discretized state-space form with N points in the wall-normal direction as

$$\mathbf{M} \frac{\partial \mathbf{q}_{k_s}(t)}{\partial t} = \mathbf{A}_{k_s} \mathbf{q}_{k_s}(t) + \mathbf{B} \mathbf{f}_{k_s}(t), \tag{2.5a}$$

$$\mathbf{m}_{k_s}(t) = \mathbf{C} \mathbf{q}_{k_s}(t) + \mathbf{n}_{k_s}(t), \tag{2.5b}$$

where $\mathbf{q}_{k_s}(t) = [\mathbf{u}_{k_s}^T(t), p_{k_s}(t)]^T$, $\mathbf{m}_{k_s}(t) \in \mathbb{C}^{N_m}$ is the system observation, $\mathbf{n}_{k_s}(t) \in \mathbb{C}^{N_m}$ is the measurement noise and N_m is the number of observations. The expressions of the operators \mathbf{M} , \mathbf{A}_{k_s} , \mathbf{B} and \mathbf{C} are provided in [Appendix A](#). Further, taking the Fourier transformation to (2.5a) in the temporal direction, the following linear relationship at each spatio-temporal scale $\mathbf{k} = (k_s, \omega)$ holds,

$$\hat{\mathbf{q}}_{\mathbf{k}} = \mathbf{H}_{\mathbf{k}} \cdot \hat{\mathbf{B}} \hat{\mathbf{f}}_{\mathbf{k}}, \tag{2.6}$$

where $\hat{\mathbf{q}}_{\mathbf{k}} = [\hat{\mathbf{u}}_{\mathbf{k}}^T, \hat{p}_{\mathbf{k}}]^T$, $\hat{\mathbf{u}}_{\mathbf{k}}$, $\hat{p}_{\mathbf{k}}$ and $\hat{\mathbf{f}}_{\mathbf{k}}$ are the Fourier coefficients of velocity, pressure and forcing at scale \mathbf{k} , respectively, and the resolvent operator $\mathbf{H}_{\mathbf{k}}$ is expressed as,

$$\mathbf{H}_{\mathbf{k}} = (-i\omega \mathbf{M} - \mathbf{A}_{k_s})^{-1}, \tag{2.7}$$

where $i = \sqrt{-1}$. From (2.6), the velocity $\hat{\mathbf{u}}_{\mathbf{k}}$ and pressure $\hat{p}_{\mathbf{k}}$ are regarded as the response of the input forcing $\hat{\mathbf{f}}_{\mathbf{k}}$ through the linear operator $\mathbf{H}_{\mathbf{k}}$. Since we will focus on predicting the velocity field in this study, the linearized equation (2.7) can be reduced to the following form:

$$\hat{\mathbf{u}}_{\mathbf{k}} = \mathbf{R}_{\mathbf{k}} \cdot \hat{\mathbf{f}}_{\mathbf{k}}, \tag{2.8}$$

where $\mathbf{R}_{\mathbf{k}}$ is obtained from $\mathbf{H}_{\mathbf{k}}$ by deleting the rows corresponding to $\hat{p}_{\mathbf{k}}$ at the left-hand side of (2.7) and columns corresponding to the constant 0 at the right-hand side. A typical application of (2.8) is to approximate the coherent structures of turbulence using the resolvent modes, which are obtained by taking the singular value decomposition to $\mathbf{R}_{\mathbf{k}}$, i.e.

$$\begin{aligned} \hat{\mathbf{u}}_{\mathbf{k}} &= \sum_{j=1}^{\infty} \left(\hat{\Psi}_{k,j} \sigma_{k,j} \hat{\Phi}_{k,j}^* \right) \cdot \hat{\mathbf{f}}_{\mathbf{k}} = \sum_{j=1}^{\infty} \sigma_{k,j} \hat{\Psi}_{k,j} \left(\hat{\Phi}_{k,j}^* \cdot \hat{\mathbf{f}}_{\mathbf{k}} \right) \\ &= \sum_{j=1}^{\infty} \sigma_{k,j} \hat{\Psi}_{k,j} \beta_{k,j}, \end{aligned} \tag{2.9}$$

where $\sum_{j=1}^{\infty} (\hat{\Psi}_{k,j} \sigma_{k,j} \hat{\Phi}_{k,j}^*) = \mathbf{R}_{\mathbf{k}}$ is the result of singular value decomposition of the resolvent operator $\mathbf{R}_{\mathbf{k}}$, the response mode $\hat{\Psi}_{k,j}$ and forcing mode $\hat{\Phi}_{k,j}$ are ordered by their singular value $\sigma_{k,j}$, the expansion coefficient $\beta_{k,j} = (\hat{\Phi}_{k,j}^* \cdot \hat{\mathbf{f}}_{\mathbf{k}})$ is the projection of forcing on the j th resolvent forcing mode and the superscript $*$ denotes the Hermitian transpose.

Using (2.8), the CSD tensors can be calculated as

$$\mathbf{S}_{uu,k} = \langle \hat{\mathbf{u}}_{\mathbf{k}} \hat{\mathbf{u}}_{\mathbf{k}}^* \rangle = \mathbf{R}_{\mathbf{k}} \cdot \left\langle \hat{\mathbf{f}}_{\mathbf{k}} \hat{\mathbf{f}}_{\mathbf{k}}^* \right\rangle \cdot \mathbf{R}_{\mathbf{k}}^* = \mathbf{R}_{\mathbf{k}} \mathbf{S}_{ff,k} \mathbf{R}_{\mathbf{k}}^*, \tag{2.10}$$

where $\langle \cdot \rangle$ denotes the ensemble average. As in (2.10), the CSD tensor of the response is fully determined when the forcing CSD $\mathbf{S}_{ff,k}$ is known. Thus, in many existing methods (e.g. Morra *et al.* 2019; Towne *et al.* 2020; Gupta *et al.* 2021), the estimating or modelling object is actually $\mathbf{S}_{ff,k}$, after which the response $\mathbf{S}_{uu,k}$ can be directly derived from $\mathbf{S}_{ff,k}$ via (2.10). In the following, the typical methods that make use of the resolvent analysis to predict the turbulence field will be introduced.

2.2. The white-noise-based estimation

With the simplest assumption, the portion of forcing that excludes the eddy-viscosity terms, as defined in (2.2), can be modelled to be white as in some research (Hwang & Cossu 2010; Madhusudanan *et al.* 2019; Morra *et al.* 2019), which means it is spatially uniform and uncorrelated. Note that, in this approach, the total forcing as defined by McKeon & Sharma (2010) is the summation of the eddy-viscosity portion and the white-noise-assumed portion. With the white-noise assumption of the WBE approach, the CSD tensor of forcing at each scale k can be expressed as

$$\mathbf{S}_{ff,k,WBE} = E_k \mathbf{I}, \tag{2.11}$$

where E_k , as the energy of forcing, keeps constant at each node and in each direction. Substituting (2.11) into (2.10) and considering the resolvent modes in (2.9), it can be deduced that

$$\mathbf{S}_{uu,k,WBE} = E_k (\mathbf{R}_k \mathbf{R}_k^*) = E_k \sum_{j=1}^{\infty} \sigma_{k,j}^2 (\hat{\Psi}_{k,j} \hat{\Psi}_{k,j}^*). \tag{2.12}$$

If we define $(\hat{\Psi}_{k,j} \hat{\Psi}_{k,j}^*)$ as the CSD of the response at the j th mode, the resultant response CSD can be interpreted as the linear summation of the CSDs of all the resolvent modes weighted by the gains $\sigma_{k,j}^2$. The white forcing, as the simplest form, can be utilized to estimate the coherent structures (Hwang & Cossu 2010; Madhusudanan *et al.* 2019; Gupta *et al.* 2021) and the spectra of turbulence (Morra *et al.* 2019). However, the resultant accuracy of prediction with the initial white forcing is far from engineering usage (Towne *et al.* 2020) even if the forcing is partially modelled by the eddy-viscosity term.

2.3. The wall-distance-dependent and scale-dependent models

To improve the prediction accuracy of the white forcing, Gupta *et al.* (2021) propose the W-model and scale-dependent model (λ -model) by modifying the profile of the forcing according to the profile of the eddy viscosity and the flow scales. The W-model and λ -model maintain the diagonal property of $\mathbf{S}_{ff,k}$ as in (2.11), while modifying the vertical energy distribution. Extended from the work of Jovanović & Bamieh (2005) in laminar flow, Gupta *et al.* (2021) propose the W-model by assuming that the vertical profile of forcing energy is proportional to that of the eddy viscosity, i.e.

$$\mathbf{w}_k = E_k \mathbf{v}_l, \tag{2.13}$$

where \mathbf{w}_k denotes the diagonal of $\mathbf{S}_{ff,k}$, i.e. the energy profile of forcing at k . Based on the fact that the nonlinear interaction of turbulence is scale dependent (Cho, Hwang & Choi 2018), Gupta *et al.* (2021) further propose the λ -model with the modified eddy viscosity, i.e.

$$\mathbf{v}_{l,k} = \frac{\lambda}{\lambda + \lambda_m} \mathbf{v}_l, \tag{2.14}$$

where $\lambda = 2\pi/(k_x^2 + k_z^2)^{0.5}$, and $\lambda_m(y) = 50/Re_\tau + (2 - 50/Re_\tau)\tanh(6y)$. The forcing energy profile is thereby calculated by $\mathbf{w}_k = E_k \mathbf{v}_{l,k}$. The strategies of modifying the forcing profiles by Gupta *et al.* (2021) efficiently improve the prediction of the vertical spatial correlation of streamwise velocity fluctuations in turbulent channel flow. However, the W-model and λ -model cannot accurately predict the energy distribution of velocity fluctuation in the near-wall region, as will be further discussed in the following sections.

2.4. The resolvent-based estimation

The RBE method (Towne *et al.* 2020) estimates the minimum L2-norm forcing that can fully recover the measured signal. Denoting \mathbf{m} as the measured set of variables and \mathbf{u} as the complete set of variables from all across the computational domain, where $\mathbf{m} = \mathcal{C}\mathbf{u}$, the RBE could be briefly expressed as

$$\mathbf{S}_{ff,k,RBE} = \mathbf{T}_{ff,k} \cdot \mathbf{S}_{mm,k} \cdot \mathbf{T}_{ff,k}^* \quad (2.15)$$

where the estimation operator $\mathbf{T}_{ff,k} = (\mathcal{C}\mathbf{R}_k)^\dagger$, $\mathbf{S}_{mm,k} = \mathcal{C}\mathbf{S}_{uu,k}\mathcal{C}^T$ is the CSD tensor of the measured variables at scale k , $\mathbf{S}_{ff,k,RBE}$ is the estimated CSD tensor of forcing, the expression of the observation matrix \mathcal{C} can be found in (A8) in Appendix A and the superscript \dagger denotes the pseudo-inverse. With the estimated forcing, the CSD tensor of the complete set of variable \mathbf{u} is calculated by

$$\mathbf{S}_{uu,k,RBE} = \mathbf{R}_k \mathbf{S}_{ff,k,RBE} \mathbf{R}_k^* \quad (2.16)$$

The RBE has been validated to be efficient for predicting the field where the turbulence is highly correlated with the measured reference points (Towne *et al.* 2020; Yang *et al.* 2020). On the other hand, since the RBE method only estimates the ‘observed’ forcing, its prediction deteriorates with the decrease of correlation between the signals of measurements and the predicted locations.

Later, Martini *et al.* (2020) demonstrate that the estimated forcing in the original version of RBE in (2.15) is actually the stationary point of the error matrix $\hat{\mathbf{e}}_{f,k} \hat{\mathbf{e}}_{f,k}^\dagger$, where the error $\hat{\mathbf{e}}_{f,k}$ is defined as the difference between the estimated forcing and the white-noise-assumed forcing here. Since the real forcing is not white, the estimation of the original RBE is not optimal to minimize the relative error between the estimated forcing and the real one. Martini *et al.* (2020) then propose the improved RBE that incorporates the effect of the forcing colour and the measurement noise, i.e.

$$\mathbf{T}_{ff,k,opt} = \mathbf{S}_{ff,k} (\mathcal{C}\mathbf{R}_k)^\dagger \left[(\mathcal{C}\mathbf{R}_k) \mathbf{S}_{ff,k} (\mathcal{C}\mathbf{R}_k)^\dagger + \mathbf{S}_{nn,k} \right]^{-1} \quad (2.17)$$

by which the stationary point of the error matrix $\hat{\mathbf{e}}_{f,k} \hat{\mathbf{e}}_{f,k}^\dagger$ between the estimated forcing and the real one is obtained. Here, $\mathbf{S}_{nn,k}$ is the CSD tensor of the measurement noise at scale k , which is set as zero since the DNS data at a given reference layer can be directly provided as measurements without introducing additional errors in this study. When the real forcing colour from additional sensors is used to inform the transfer function, the optimized RBE performs better than the original RBE in estimating the turbulent channel flow given the same amount of measurements. However, the optimized RBE needs the knowledge of forcing statistics obtained from additional sensors or forcing models, which is not considered in this study. Thus, the RBE method mentioned in the following refers to its original version by Towne *et al.* (2020), which will be used to develop our newly proposed methods and provide comparison results.

The above existing methods can be categorized into two groups. First, the WBE, W-model and λ -model assume that the forcing is uncorrelated in space, then explicitly model the forcing energy with predefined profiles. These approaches aim to describe the forcing statistics throughout the flow field. On the other hand, the information of the measurements is only utilized to determine the overall forcing energy E_k , while the estimated relative energy distribution of forcing is independent of the measurements. The advantage of these methods with predefined profiles is that the predicted response can

generally reflect the energy distribution of the response to some extent, no matter how far the measurement layers are located from the prediction region. However, the performance of the prediction is highly dependent on the specific form of the predefined profiles, which implies that the accuracy of this group of methods could not be as good as expected, even if the measurements and predictions are close to each other, as can be seen in §4. Second, the RBE infers the forcing statistics from the measurements without imposing assumptions on the form of the forcing profile. The RBE has been validated to be efficient for predicting the field where the turbulence is highly correlated with the measured reference points (Towne *et al.* 2020; Yang *et al.* 2020). However, since it only estimates the ‘observed’ forcing, its prediction accuracy deteriorates with increasing distance between the measurements and the predicted locations.

3. Derivations of the resolvent-informed white-noise-based estimation method

From the above discussions of the existing methods, the group of methods assuming predefined profiles and the RBE compensate with each other in a sense. Specifically, the group of methods assuming predefined profiles performs better in estimating the general energy distribution of the forcing and response when there is a long distance between the measurements and the prediction region. On the other hand, the RBE is efficient in providing reasonable estimations when the measurements are located near the prediction. According to Holford, Lee & Hwang (2023), the energy spectra of turbulence can be well recovered using the spatially uncorrelated forcing with optimal profiles. In this study, following the strategy of modifying the spatially uncorrelated forcing profile, we aim to propose an adaptive method to adjust the spatially uniform and uncorrelated forcing profile based on reliable inference informed by the RBE.

As already discussed, when the measured reference layer is not close to the prediction region, the RBE cannot be directly applied for prediction due to the deterioration of accuracy. However, the RBE can, instead, be utilized to estimate the relative energy profile of the response with respect to an assumed reference layer that is closer to the wall than the actual reference layer. Based on the basic RBE formula (2.15)–(2.16), the predicted relative CSD tensor of velocity u_i near the wall can be estimated as

$$\hat{\mathbf{S}}_{u_i u_i, k, RBE} = \frac{\mathbf{S}_{u_i u_i, k, RBE}}{\mathbf{S}_{mm, k}} = \mathbf{R}_k (\mathcal{C} \mathbf{R}_k)^\dagger \cdot (\mathcal{C} \mathbf{R}_k)^{\dagger*} \mathbf{R}_k^*, \quad (3.1)$$

where $\mathbf{S}_{mm, k}$ should be the scalar energy of u_i at a single reference height so that it can be eliminated from the denominator by the numerator. Note that there is no requirement on the specific value of the reference height in (3.1), a pretty high accuracy can be obtained for predicting the relative CSD tensor. This desirable property of the RBE in estimating the relative response statistics provides a standard for the modification of the initially assumed white forcing profile. To be distinguished from the actual reference layer, which is denoted as y_R , the assumed reference layer used for estimating the relative CSDs in (3.1) is denoted as the quasi-reference layer y_Q in this article. To obtain the relative CSD tensor used for the optimization, the value of y_Q should be determined first. According to Towne *et al.* (2020), the accuracy of RBE decreases as the wavenumbers and frequency increase. As the wavenumbers and frequency are closely related to the flow scale, we choose to determine the quasi-reference layer according to the flow scale in the wall-normal direction. The purpose of this step is to let the RBE provide a reasonable estimation of the widest possible wall-normal extent. To quantify the wall-normal scale, the linear coherence spectrum

(LCS) γ^2 (Baars *et al.* 2016) is introduced here, i.e.

$$\gamma^2(\mathbf{k}) = \frac{\left| \left\langle \hat{\mathbf{u}}_k(y_Q^+) \overline{\hat{\mathbf{u}}_k(y_P^+)} \right\rangle \right|^2}{\left\langle \left| \hat{\mathbf{u}}_k(y_Q^+) \right|^2 \right\rangle \left\langle \left| \hat{\mathbf{u}}_k(y_P^+) \right|^2 \right\rangle}, \quad (3.2)$$

where $\hat{\mathbf{u}}_k$ is the Fourier coefficient of \mathbf{u} at scale \mathbf{k} , the overline denotes the complex conjugate and $y_P^+ = 15$ corresponds to the height of the near-wall inner peak (Smits, McKeon & Marusic 2011). Since the LCS at a given distance increases as the flow scale enlarges, the LCS could be an effective index to quantify the flow scale. Based on the value of LCS preliminarily estimated from the WBE, the quasi-reference layer y_Q is set as the height beyond the inner peak where $\gamma^2(\mathbf{k}) = 0.3$. When the height of y_Q exceeds y_R , it will be set as y_R instead. With the above procedure, the value of y_Q is adaptively determined. Details of the implementation of the LCS calculation and discussions about the impact of the threshold LCS on the prediction accuracy are provided in [Appendix C](#).

With the information of the turbulence statistics below y_Q from the RBE, our goal is to minimize the relative error between the estimated CSD of the velocity u from the modified forcing and the RBE-estimated one. As will be revealed in § 4.3, the RBE just provides the reliable prediction of the relative energy profile below the quasi-reference layer y_Q , which does not work well when $y \geq y_Q$. Thus, the modification range of the forcing is restricted below y_Q . For the region beyond the quasi-reference layer, there is no reliable information to further improve the forcing profile there. Thus, a conservative strategy is adopted by setting the forcing to be unity at each node for $y \geq y_Q$, which corresponds to the spatially uniform forcing, as also assumed by the WBE reviewed in § 2.2. Derivations of the explicit relationship between the relative energy profiles of forcing and response are provided in [Appendix D](#). For each scale $\mathbf{k} = (k_x, k_z, \omega)$, the norm minimization problem is considered as follows:

$$\begin{aligned} & \underset{\mathbf{w}_k}{\text{minimize}} && \left\| \frac{\text{diag} [\mathbf{S}_{uu,k}(\mathbf{w}_k)]|_{y < y_Q}}{\text{diag} [\mathbf{S}_{uu,k}(\mathbf{w}_k)]|_{y = y_Q}} - \text{diag} [\hat{\mathbf{S}}_{uu,k,RBE}]|_{y < y_Q} \right\|, \\ & \text{subject to} && 0 \leq \mathbf{w}_k(y) \leq 1, \quad \frac{d\mathbf{w}_k(y)}{dy} \geq 0, \quad \forall y \in [0, y_Q], \\ & && \mathbf{w}_k(y) = 1, \quad \forall y \in [y_Q, 2h], \end{aligned} \quad (3.3)$$

where the norm $\|\cdot\|$ is defined as $\|\cdot\| = \int_0^{y_Q} (\cdot)^2 dy$. This constrained optimization problem is solved with the interior point method (Momoh, El-Hawary & Adapa 1999). By minimizing the norm of the error matrix, the energy spectrum of the modified response is optimized with respect to the RBE-estimated one. After the relative profile of \mathbf{w}_k is obtained from the optimization, the forcing profile will be multiplied by a unified coefficient E_k to match the response energy at the reference layer for all the velocity components of u , v and w , respectively.

The above construction process of the newly proposed RWE method is sketched in [figure 1](#). To illustrate the actual modification process of the forcing and its effects on the response energy profile, the scale with $(k_x, k_z, \omega) = (3.0/h, 30/h, 1.3u_c/h)$ corresponding to the large-scale motions (Smits *et al.* 2011) is selected, as in [figure 2](#), where u_c is the mean velocity at the half-channel height h . The forcing energy is uniformly distributed in the vertical direction before the modifications, with the corresponding response energy profile

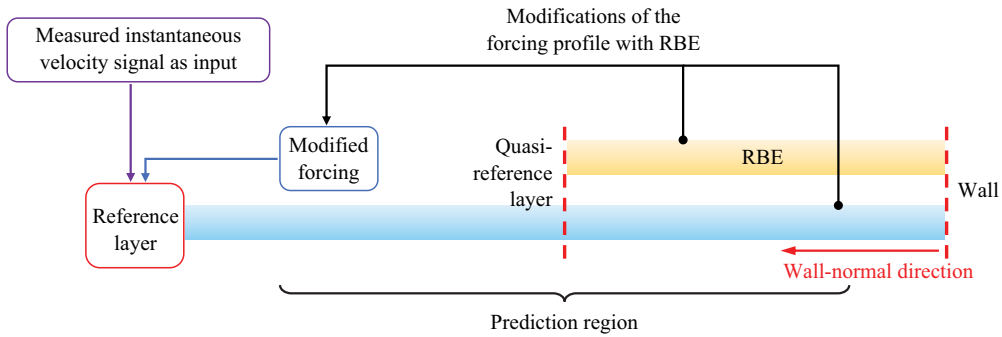


Figure 1. Schematic sketch of the white-noise-based estimation (RWE).

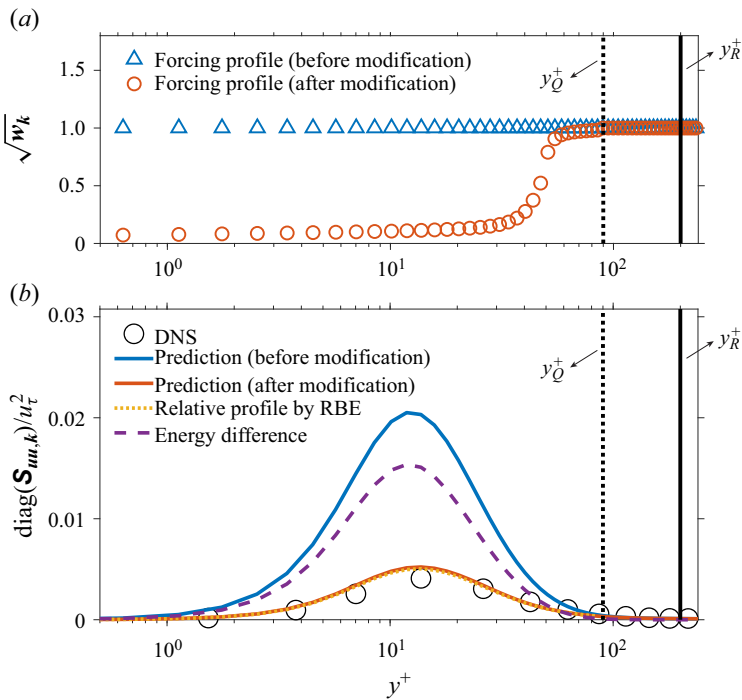


Figure 2. Sketch of the modification process at $(k_x, k_z, \omega) = (3.0/h, 30/h, 1.3u_c/h)$. (a) Energy profile of forcing. (b) Energy profile of the streamwise velocity.

much larger than the DNS results in the near-wall region, as figure 2(b). The height of the quasi-reference layer y_Q^+ is determined according to the LCS value defined in (3.2). During the modification procedure, the forcing energy is reduced in the near-wall region to let the predicted relative energy profile approach that by the RBE till the norm of the error matrix in (3.3) reaches the minimum under the constraints. The forcing and response profiles after modification are denoted in the orange colour in figures 2(a) and 2(b), respectively. The response energy profile after modification matches well with the DNS and RBE results.

In the next section, validations of the RWE will be conducted in terms of the prediction capability of the near-wall statistics as well as the instantaneous flow field with the DNS data and several representative existing prediction methods. The WBE (Morra *et al.* 2019) and RBE (Towne *et al.* 2020) will be included in the following validations, since they

Re_τ	N_x	N_z	N_y	L_x/h	L_z/h	L_y/h	$(u_\tau T)/h$
180	768	512	97	12π	4π	2	11.45
550	1536	1536	257	8π	4π	2	8.80
950	3072	2304	385	8π	3π	2	5.39

Table 1. Parameters of the incompressible channel DNS set-ups.

provide the initial forcing profile and the reference for optimization for the newly proposed RWE method, respectively. Besides, the λ -model (Gupta *et al.* 2021) considers the effects of flow scale on the estimated forcing profile, which is found to perform better than the W-model and WBE (named the B-model by Gupta *et al.* 2021) for estimating the large-scale motions in the near-wall region. Thus, the λ -model will also be included in the following validations. Note that the λ -model is originally used in cases where temporal information of velocity is unknown. The forcing is thus assumed to be white in time in those cases (Gupta *et al.* 2021), the response CSD tensor of which can be obtained via the algebraic Lyapunov equation. Meanwhile, in this study, the λ -model will be applied in the time-resolved cases instead, where the flow is estimated at each spatio-temporal scale quantified by $\mathbf{k} = (k_x, k_z, \omega)$. The modified eddy viscosity and forcing profiles in the λ -model will be calculated by (2.14) at each scale (k_x, k_z) , keeping consistent with the original version.

4. Results

In this section, the DNS data with three friction Reynolds numbers equal to 180, 550 and 950 are used to provide reference measurements at corresponding locations and validate the tested methods in predicting the flow properties of turbulent channel flows.

4.1. Descriptions of the DNS database

The code used to compute the extensively validated DNS database for channel flows (Del Alamo & Jiménez 2003; Hoyas & Jiménez 2008) is utilized to generate the time-resolved channel flow data with $Re_\tau = 180, 550$ and 950 . Details of the DNS set-ups are listed in table 1. To provide time-resolved results, the sampling time intervals $\Delta t^+ = (\Delta t)u_\tau^2/\nu$ are set as 2.13, 4.81 and 5.09 for cases with $Re_\tau = 180, 550$ and 950 , respectively. The normalized total simulation time $(u_\tau T)/h$ is larger than 5.0 in each case to obtain statistically convergent results. To assess the DNS dataset generated in this study, comparisons of the mean and root-mean-squared velocity profiles with the open source DNS database (Del Alamo & Jiménez 2003; Hoyas & Jiménez 2008) are provided in Appendix B.

To process the DNS data, the flow field is divided into blocks with a spatial domain of sizes $L_x/h = 4\pi$, $L_z/h = \pi$ and $L_y/h = 1$ in each case. Given that the turbulent channel flow is statistically symmetric about the centreline $y = h$, the flow data at $y = y_0$ will be utilized together with those at $y = 2h - y_0$ when investigating the flow at $y = y_0$. The time periods of the blocks are set as $80\Delta t$, $80\Delta t$ and $120\Delta t$ for cases with $Re_\tau = 180, 550$ and 950 , respectively, with 75 % overlap in the temporal direction. The rectangular window function is used when conducting spectral analyses. With the above set-ups for data processing, the numbers of blocks are 1128, 752 and 360 for cases with $Re_\tau = 180, 550$ and 950 , respectively.

Case	180-40	550-40	550-100	950-40	950-100	950-200
Re_τ	180	550	550	950	950	950
y_R^+	40	40	100	40	100	200
y_R/h	0.22	0.073	0.18	0.042	0.11	0.21

Table 2. Case settings for validation.

4.2. Case settings

Six cases are set to validate the prediction methods, as summarized in table 2. Besides the Reynolds number Re_τ , the height of the reference layer y_R where the measurements are obtained is also treated as an independent variable to test the sensitivities of the methods to the location of measurements, which ranges from the near-wall region at $y^+ = 40$ to the upper bound of the logarithmic region at $y/h \approx 0.2$. The wall-normal direction y is discretized with 129, 201 and 257 Chebyshev polynomials in cases with $Re_\tau = 180, 550$ and 950, respectively, with no-slip boundary conditions applied at the walls.

4.3. Reynolds stress profiles

In this section, the root-mean-squared (r.m.s.) velocities and the Reynolds shear stress (RSS) are investigated to study the ensemble effect of fluctuations with all the spatio-temporal scales along the height. Specifically, the r.m.s. velocities quantify the fluctuation energies of u' , v' and w' , which are important indexes to validate the DNS (e.g. Cheng *et al.* 2019) or prediction methods (e.g. Towne *et al.* 2020). On the other hand, the RSS $\langle u'v' \rangle$ quantifies the correlation of u' and v' , which is closely related to the skin friction of wall-bounded turbulence (Fukagata, Iwamoto & Kasagi 2002) and has been investigated via the resolvent analysis for flow control (Luhar, Sharma & McKeon 2015; Nakashima, Fukagata & Luhar 2017).

When $Re_\tau = 180$, the only reference layer at $y^+ = 40$ is used for the predictions. According to the evaluations of RBE by Yang *et al.* (2020), the best performance of RBE in terms of estimating the r.m.s. profile of the streamwise velocity is achieved when $y^+ = 39$, which is very close to $y^+ = 40$ used in the current case. As in figure 3(a), the r.m.s. profiles predicted by RBE are pretty consistent with the DNS results in all three directions, with only 2.0 % relative error at the inner peak of the streamwise r.m.s. velocity profile. The RWE also performs well when $Re_\tau = 180$ with a relative error of 13.2 % at the inner peak. On the other hand, the predictions from the λ -model and WBE both deviate quite a lot from the DNS results, with maximum errors of 25.7 % and 109.7 % at the inner peaks of the streamwise r.m.s. velocity. Note that this case is considered to be the least challenging one with the smallest Reynolds number and the closest reference layer to the wall, the large prediction errors in the λ -model and WBE results indicate that the predefined forcing profiles cannot properly model the forcing effects if not adjusted by additional flow information, especially in the near-wall region.

With the increase of Re_τ , the RBE continues performing well when the reference layers are located at $y^+ = 40$, with the maximum error of 7.7 % at the inner peak in case 950-40. However, as the reference layer moves away from the wall, the RBE-predicted energy decreases rapidly, which is considered to be attributed to the decrease of coherence between the signals at the reference layer and the near-wall region. Especially, when the reference layer is located at $y^+ = 200$ with $Re_\tau = 950$, the energy peak can be barely observed in the RBE-predicted streamwise r.m.s. profile. Like the RBE, the energies

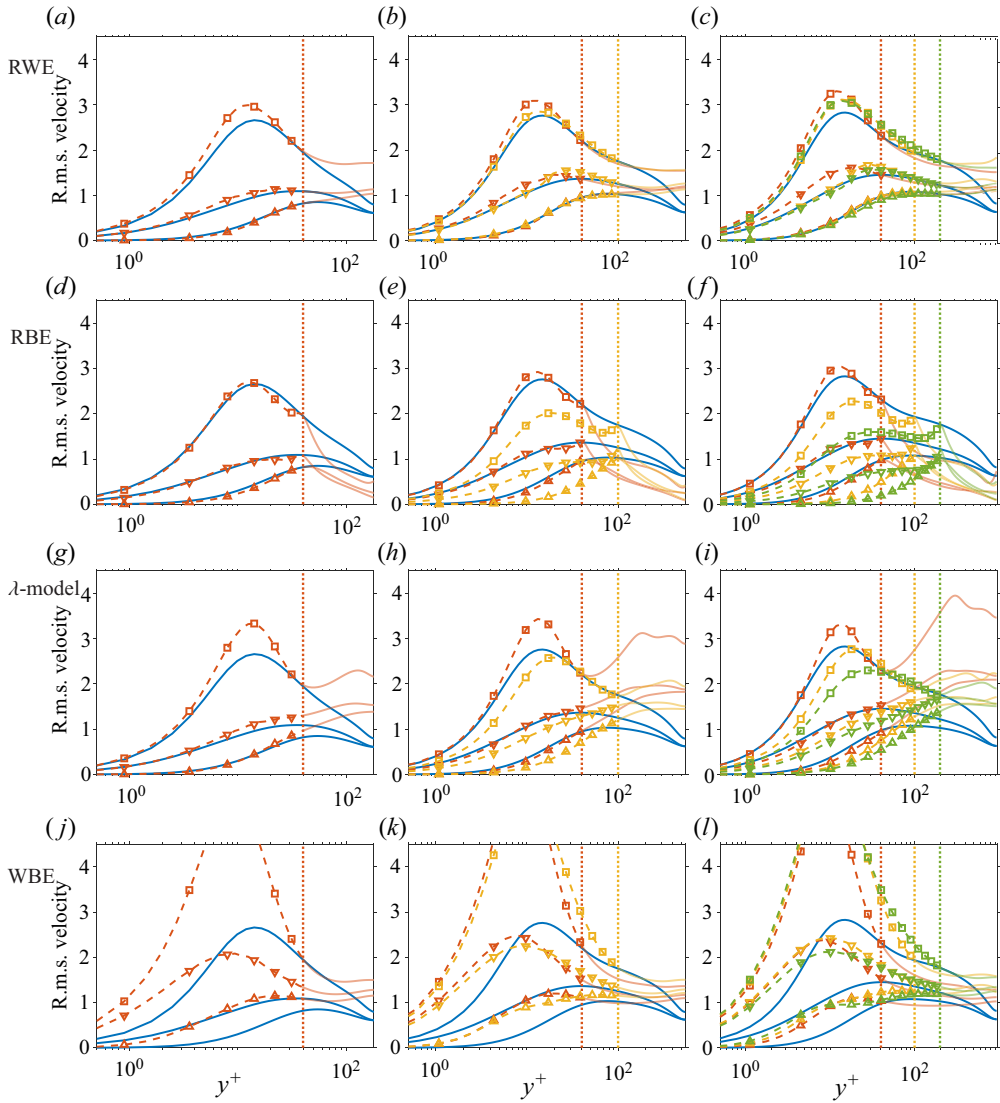


Figure 3. Comparisons of the r.m.s. profiles for cases with $Re_\tau = 180$ (a,d,g,j), 550 (b,e,h,k) and 950 (c,f,i,l). The solid lines denote the DNS results. The dashed lines denote the predictions from the RWE (a–c), λ -model (d–f), RBE (g–i) and WBE (j–l), where the lines with square, lower triangles and upper triangles denote the RMSs of the streamwise velocity, spanwise velocity and vertical velocity, respectively. The vertical dotted lines denote the reference layers corresponding to the dashed lines with the same colours.

predicted by the λ -model also tend to decrease when the reference layer lifts upward, which overestimates and underestimates the energy with $y_R^+ = 40$ and $y_R^+ = 200$, respectively. When $y_R^+ = 100$, the λ -model-predicted results match fairly well with the DNS results. The WBE overestimates the energies of the fluctuations of all the velocity components in all the tested cases, which indicates that the WBE cannot be directly used to estimate the energy magnitude in the near-wall region. Despite this, the capacity of WBE to estimate the distributions of the relative energy spectra should be further investigated in the following sections. Compared with the above methods, the RWE performs steadily

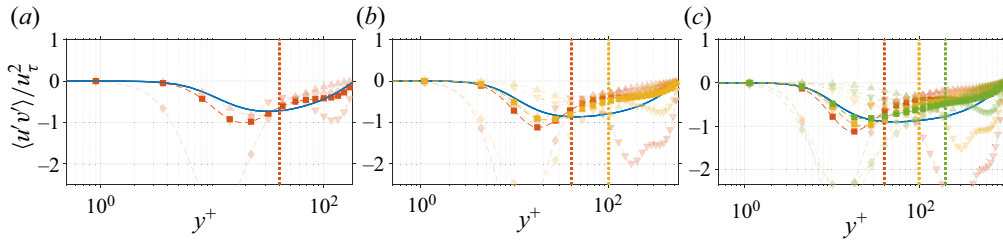


Figure 4. Comparisons of the RSS profiles for cases with $Re_\tau = 180$ (a), 550 (b) and 950 (c). The solid lines and dashed lines denote the DNS results and predictions, respectively. The lines with square, upper triangles, lower triangles and diamonds denote RWE, RBE, λ -model and WBE results, respectively, where only the RWE results are depicted with opaque colours. The vertical dotted lines denote the reference layers corresponding to the dashed lines with the same colours.

well in all the cases with various Reynolds numbers and choices of the reference layers, with the maximum error equal to 16.6% at the inner peak of streamwise r.m.s. velocity in case 950-40.

Besides the r.m.s. velocity profiles below the reference layer, those in the higher region in each case are also depicted in figure 3 with translucent curves. From the RWE results, the predicted profiles match well with the DNS results in the wall-normal range of $y \in (y_R, 0.2h)$ for all the r.m.s. velocities with different Reynolds numbers and reference layers. Moreover, for the same Reynolds number, the profiles predicted by the RWE nearly overlap with each other for each Reynolds number, which again demonstrates the insensitivity of the RWE results to the choice of reference layer. For the region that is higher than the upper bound of the logarithmic region, i.e. $y > 0.2h$, the RWE results become larger than those from the DNS, which should be attributed to the mismatch of the RWE-modelled forcing profile in the outer layer with the real forcing in the DNS results. On the other hand, the other three considered methods cannot provide satisfying results at $y > y_R$. For the RBE, the magnitudes of the r.m.s. velocities shrink rapidly when the prediction location lifts up from the reference layer. On the contrary, the λ -model results become obviously larger than the DNS results at $y > y_R$, which implies that the λ -model overestimates the forcing in the logarithmic region. The WBE underestimates the fluctuation energies at $y \in (y_R, 0.2h)$, which in turn overestimate the magnitudes in the outer layer.

The RSS profiles are depicted in figure 4. The RWE-predicted RSS profiles, which are obtained from the measurements of the streamwise velocity at the reference layers, are fairly consistent with the DNS results in all the cases. The RBE results that are depicted with upper triangles match well with the DNS results when $y_R^+ = 40$. However, when the reference layer increases to 100 and 200, the magnitudes of the RBE-predicted RSS profiles become obviously underestimated. In the meantime, the λ -model and WBE neither provide satisfying results with different Reynolds numbers and reference heights.

From the above discussions, the impacts of the friction Reynolds numbers and measuring locations on the prediction accuracy of the tested methods can be concluded as follows. When the Re_τ increases, the accuracy of prediction with the same y_R^+ by the RBE and RWE does not show an obvious difference. Meanwhile, the variation of the measuring locations significantly influences the prediction accuracy of all the methods except for the newly proposed RWE. Specifically, the increasing height of the reference layer reduces the predicted fluctuation energy at a given height for the RBE and λ -model, the errors of which become minimum when $y_R^+ = 40$ and 100, respectively. Since the measurements are usually not guaranteed to be fixed at an ideal location in the WMLES or experiments, the

insensitivity of the choices of reference layers implies a large potential of RWE to practical engineering applications.

4.4. One-dimensional energy spectra of the fluctuation velocities

Besides the r.m.s. profiles, the energy spectra, which describe the energy distributions among different scales, provide a more comprehensive picture to display the predicted flow properties. In this section, the distributions of one-dimensional energy spectra at different heights as functions of k_x , k_z or ω will be studied. For brevity, only the results of streamwise velocity u , as the most interesting physical quantity, in the cases where the reference layers are the farthest away from the wall for the corresponding Reynolds numbers, i.e. cases 180-40, 550-100 and 950-200, are chosen for the validations in this section.

Figure 5 depicts the premultiplied one-dimensional energy spectra of the streamwise velocity u with the reference layer located at $y^+ = 40$, where the location of the reference layer is denoted with the white dashed line in each case. The black dashed line denoting the contour of $0.5S_{DNS,max}$ is marked in each case to highlight the energy-concentrating region, where $S_{DNS,max}$ is the maximum premultiplied spectral energy of the DNS result in the same case. The values of the premultiplied energy are normalized by $S_{DNS,max}$. When the reference layer is located at $y^+ = 40$ with $Re_\tau = 180$, the RBE works well in predicting the energy distributions at different heights and flow scales, with the maximum error lower than $0.25S_{DNS,max}$ according to figure 6, that depicts the relative error. This result is consistent with the previous work that also uses the RBE to predict the energy spectra with the reference layer at $y^+ = 37$ (Towne *et al.* 2020). The energies predicted by the RWE also match fairly well with the DNS results, whose maximum error is approximately $0.46S_{DNS,max}$. On the other hand, the relative errors that are larger than $1.0S_{DNS,max}$ are observed in the results of the λ -model and WBE. For the λ -model, the maximum error occurs at the heights around the inner peak $y^+ = 15$ and the scales that are slightly smaller than the energy-concentrating scales predicted by the DNS, as denoted by the black dashed lines. This indicates that the deviations between the λ -model and DNS results mainly concentrate at small scales near the inner peak. On the other hand, the WBE overestimates the energy within a wide wall-normal range from $y^+ = 3$ to 20, which indicates that the WBE results cannot be directly applied to the predictions of the magnitude of the energy spectra.

Although the WBE overestimates the magnitude of the energy, it is still worth investigating the relative spectral energy predicted by the WBE. To depict the relative spectral energy distributions in the WBE results, we set the upper bound of the colour bar as the maximum spectral energy predicted by the WBE rather than $S_{DNS,max}$. The relative distributions of the energies predicted by WBE are roughly consistent with those from the DNS, while deviations could also be found, e.g. the inner peak for the streamwise velocity from WBE is located at about $y^+ \approx 10$, which should be at $y^+ \approx 15$ according to the DNS results.

Among the above-discussed methods, the RBE provides the most accurate results, followed by the RWE. Although the RWE result does not totally recover the RBE results, it provides a better result over the WBE and λ -model.

With the increase of the reference height y_R , as in figures 7–10, the prediction accuracy of RBE deteriorates obviously. The RBE-predicted energy-concentrating regions denoted by the black dashed lines shrink towards the vicinity around $y^+ = 15$ in case 550-100, which finally disappear in case 950-200, indicating that the near-wall energy is seriously underestimated by RBE when $y_R^+ = 200$. On the other hand, as the reference layer lifts

Resolvent-based prediction with limited measurements

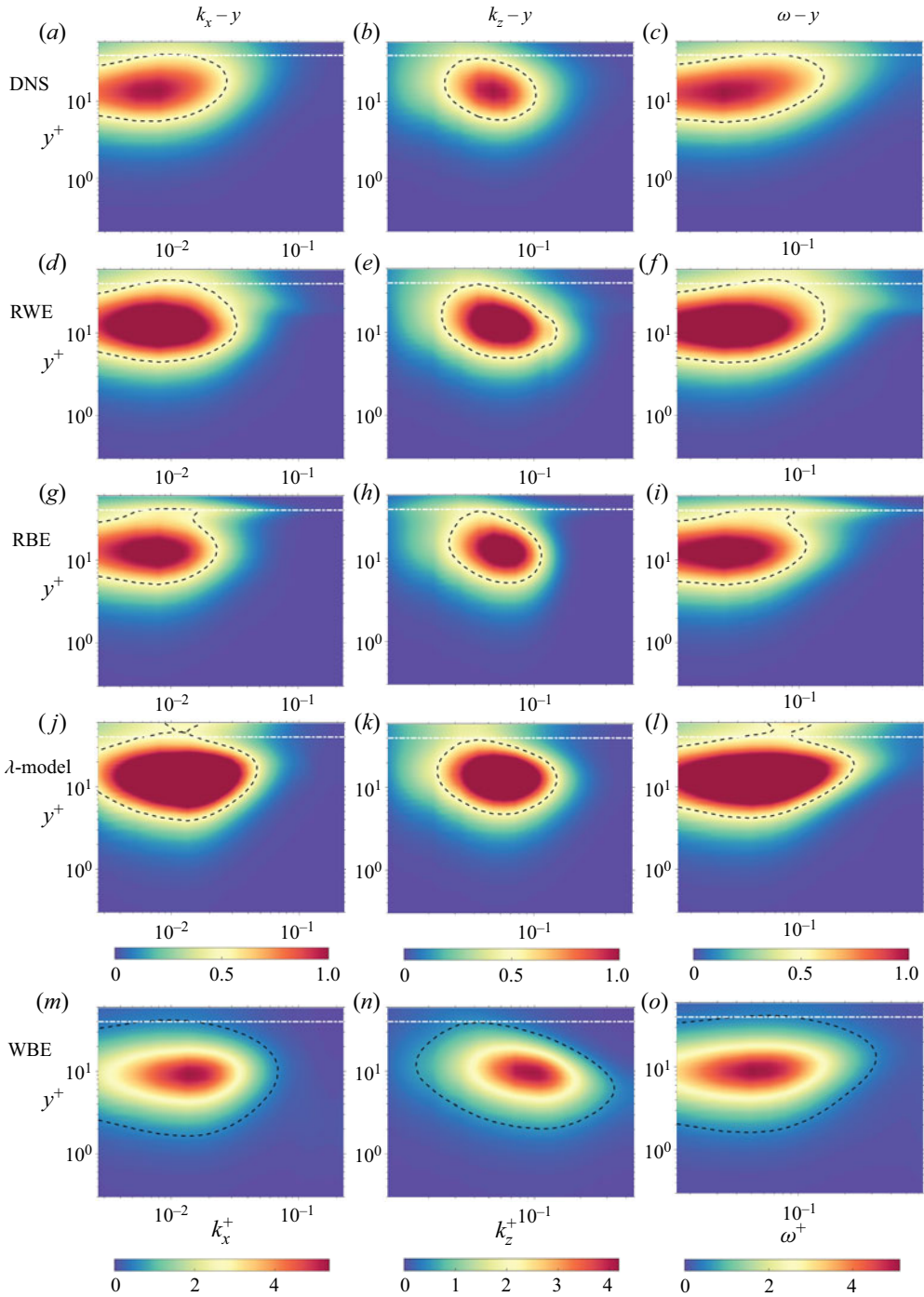


Figure 5. Premultiplied energy spectra of streamwise velocity as a function of the wall-normal distance y and the streamwise wavenumber k_x (a,d,g,j,m), spanwise wavenumber k_z (b,e,h,k,n) and frequency ω (c,f,i,l,o) in case 180-40, from the results of DNS (a–c), RWE (d–f), RBE (g–i), λ -model (j–l) and WBE (m–o). The black dashed lines denote the contour of $0.5S_{DNS,max}$, and the white dash-dotted lines denote the height of the reference layer. The values shown in the figures are normalized by $S_{DNS,max}$.

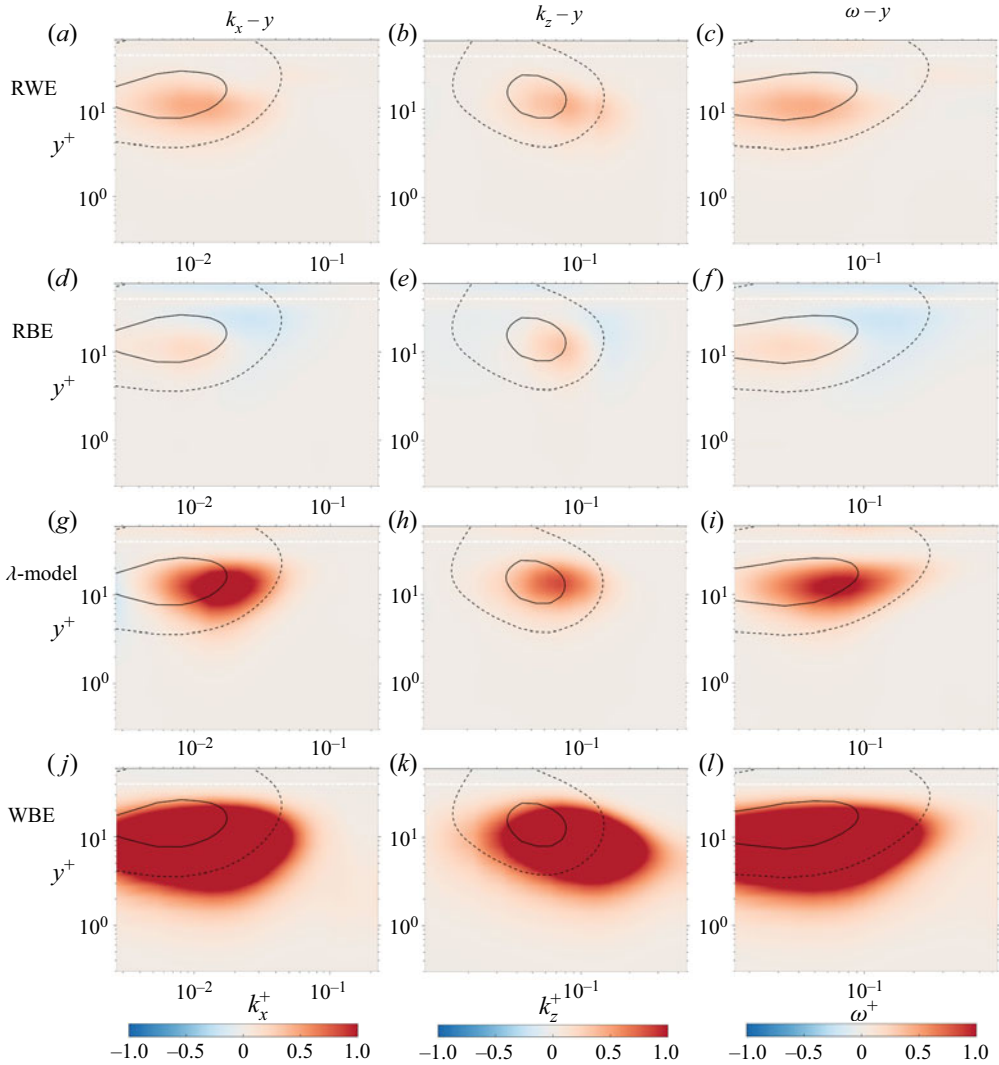


Figure 6. Relative error of the premultiplied energy spectra of streamwise velocity as a function of the wall-normal distance y and the streamwise wavenumber k_x (a,d,g,j,m), spanwise wavenumber k_z (b,e,h,k,n) and frequency ω (c,f,i,l,o) in case 180-40, from the results of DNS (a–c), RWE (d–f), RBE (g–i), λ -model (j–l) and WBE (m–o). The values shown in the figures are normalized by $S_{DNS,max}$. The black solid and dashed lines denote the contours of $0.75S_{DNS,max}$ and $0.25S_{DNS,max}$, respectively.

up, the magnitude of the λ -model-predicted energy decreases gradually. In case 550-100, the λ -model results match well with the DNS results, with the relative error lower than $0.35S_{DNS,max}$, as in figure 8. When y_R^+ increases to 200, the energy magnitude predicted by the λ -model continues decreasing and consequently becomes lower than the DNS results by more than $0.75S_{DNS,max}$ in the small scales at around $y^+ = 15$, as in figure 10. The WBE significantly overestimates the magnitude of energy, while the relative energy distribution roughly reflects the patterns of the DNS results. Compared with the WBE, the λ -model has a higher accuracy, which highlights the importance of including the scale effects when determining the forcing profile. Meanwhile, the RWE keeps the highest accuracy in the streamwise energy distributions with k_x^+ , k_z^+ , and ω^+ , with the maximum error of

Resolvent-based prediction with limited measurements

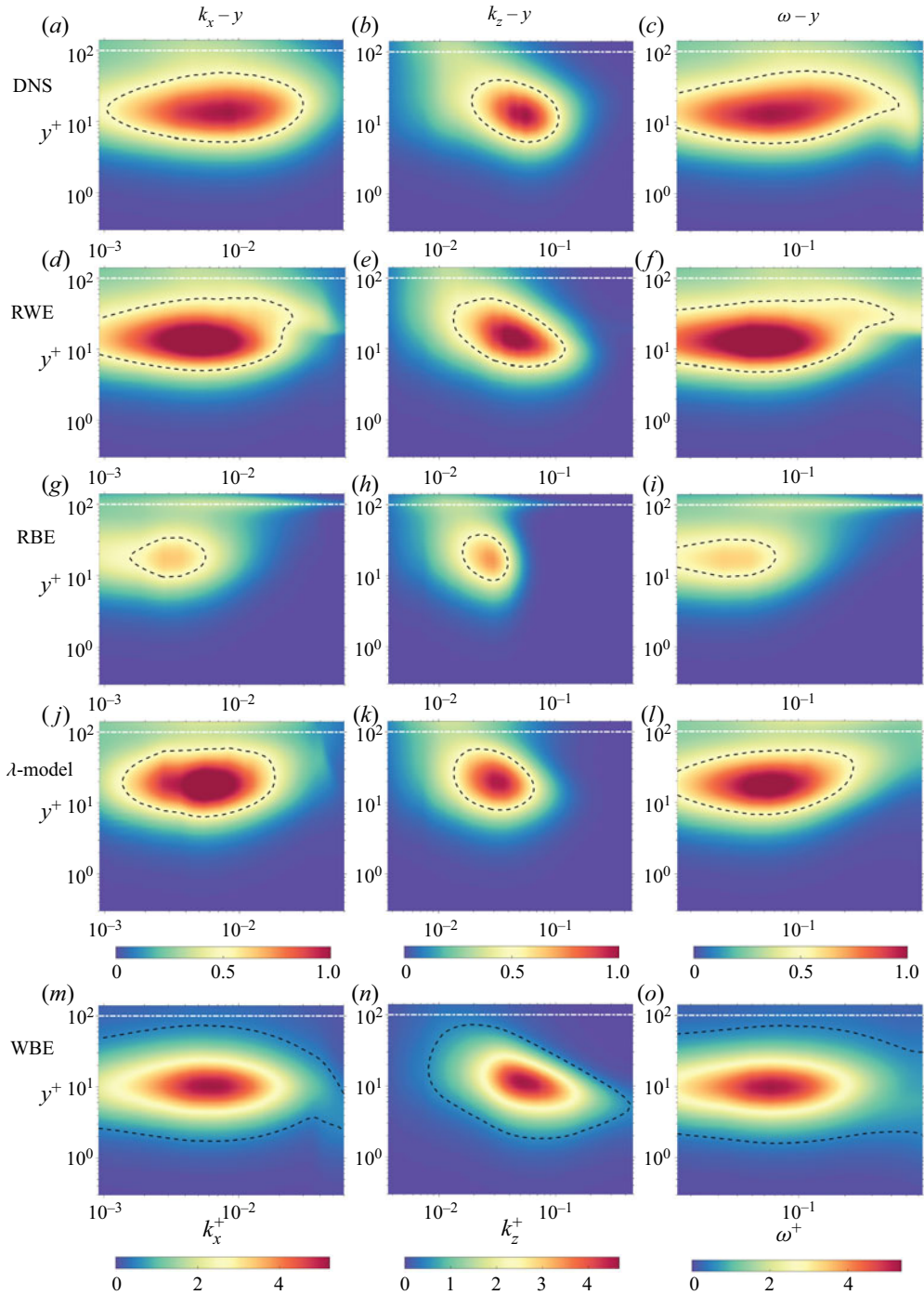


Figure 7. Same as figure 5, but in case 550-100.

$0.33S_{DNS,max}$. The good performance of the RWE supports the capability of the adaptive modification process as derived in § 3.

In order to quantitatively analyse the patterns of the near-wall predictions from different methods as the reference layer moves away from the wall, the relative errors at the inner

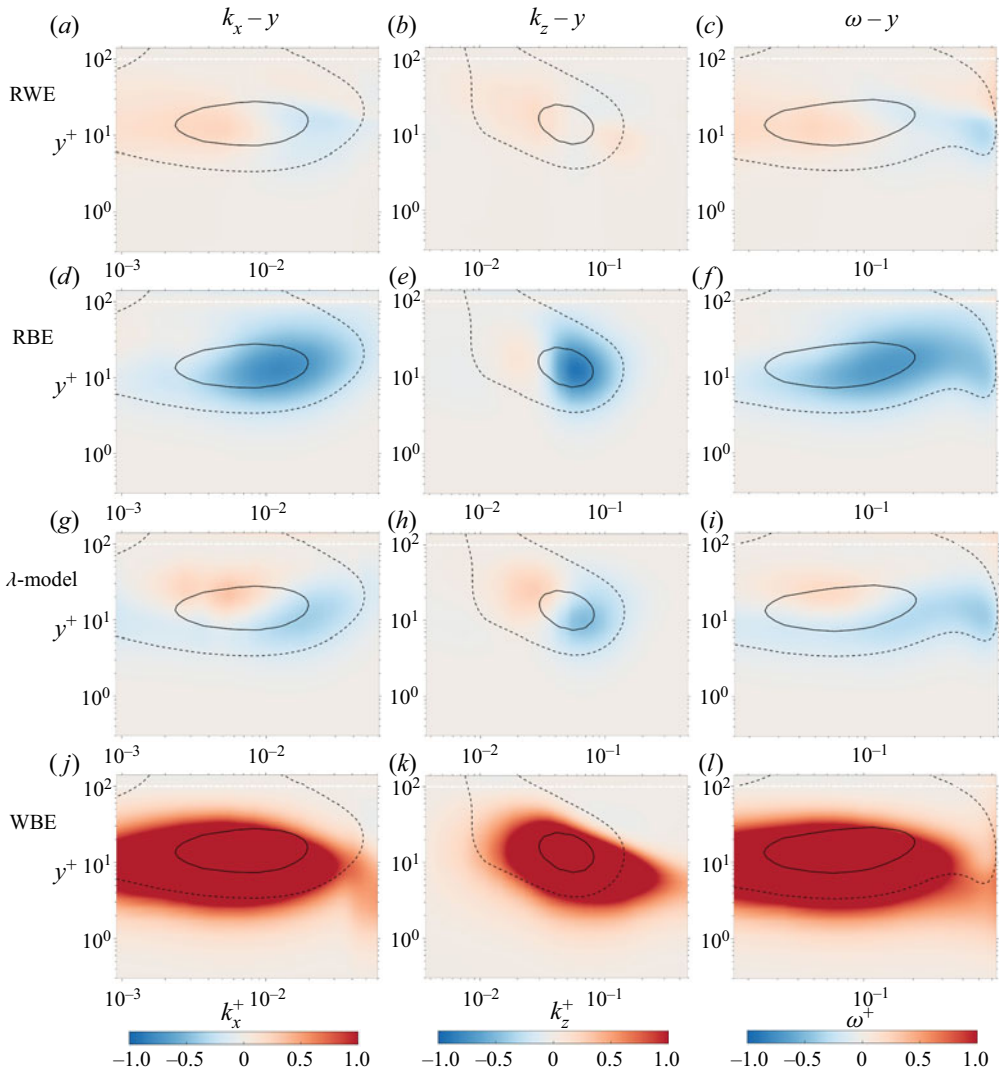


Figure 8. Same as figure 6, but in case 550-100.

peak ($y^+ = 15$) and along different scales quantified by k_x^+ , k_z^+ and ω^+ are shown in figure 11. The values are normalized by $S_{DNS,max}$, as consistent with those in figures 6, 8 and 10. The green curves denoting the relative errors of the WBE results deviate too much from the reference zero value, and thus they cannot be fully depicted in the figures. The predicted energies from the RBE and λ -model show a clear trend to decrease compared with the DNS results as the reference layer lifts up. For instance, in case 180-40, the spectral energy predicted by the λ -model is larger than the DNS results at almost all the scales, whose maximum error is more than $1.37S_{DNS,max}$ with a positive value. When the reference layer lifts up to $y^+ = 200$, the maximum relative error of the λ -model predictions becomes $0.7S_{DNS,max}$ with a negative value instead. With the increasing height of the reference layer, the RBE and λ -model achieve their best performance with $y_R^+ = 40$ and 100, respectively. On the other hand, the relative error of the RWE results is pretty small in the cases tested. Meanwhile, with the increase of flow scales, the spectral energy

Resolvent-based prediction with limited measurements

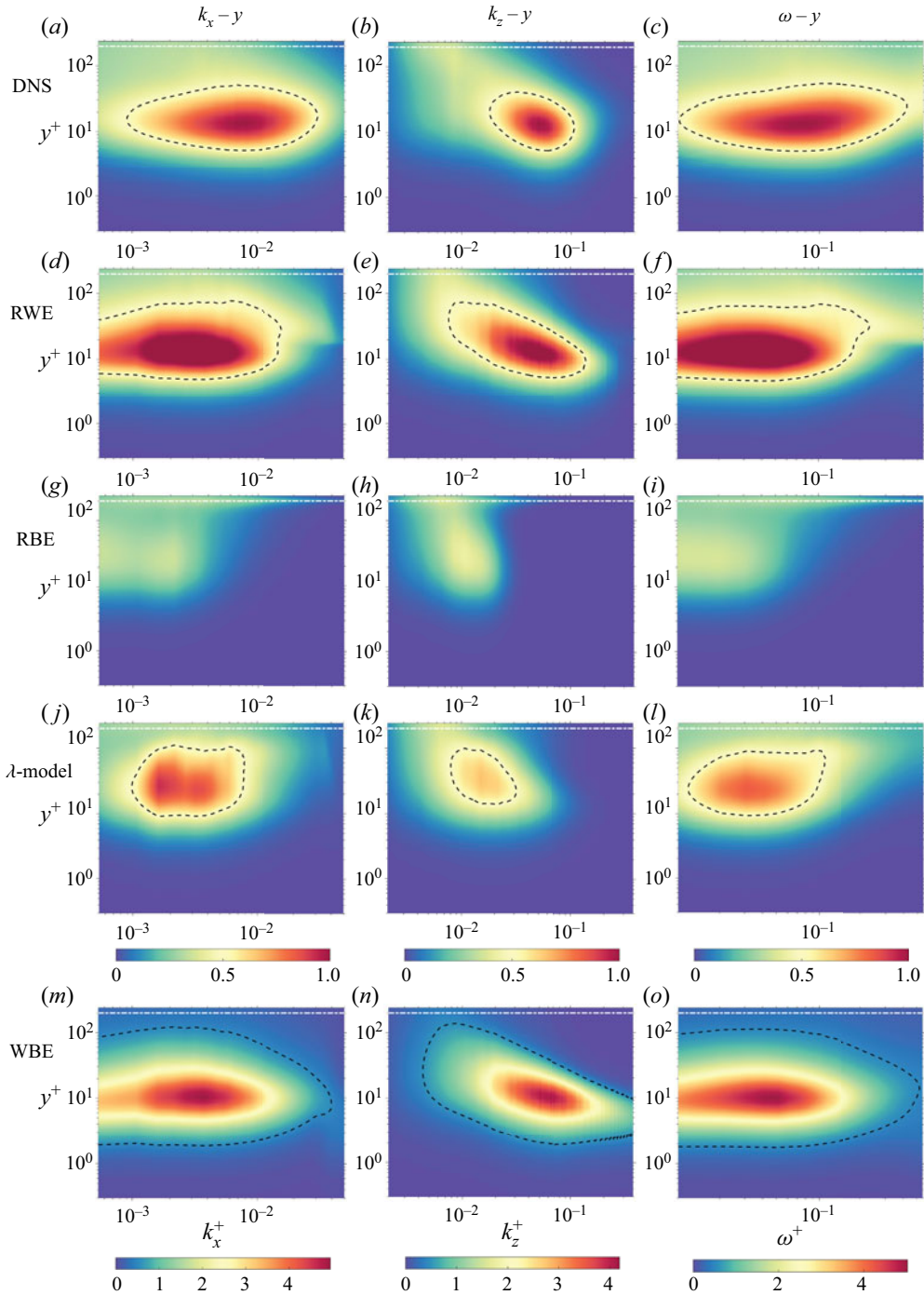


Figure 9. Same as figure 5, but in case 950-200.

predicted by the RWE tends to increase compared with the DNS results, which can also be observed in the predictions from the other tested methods.

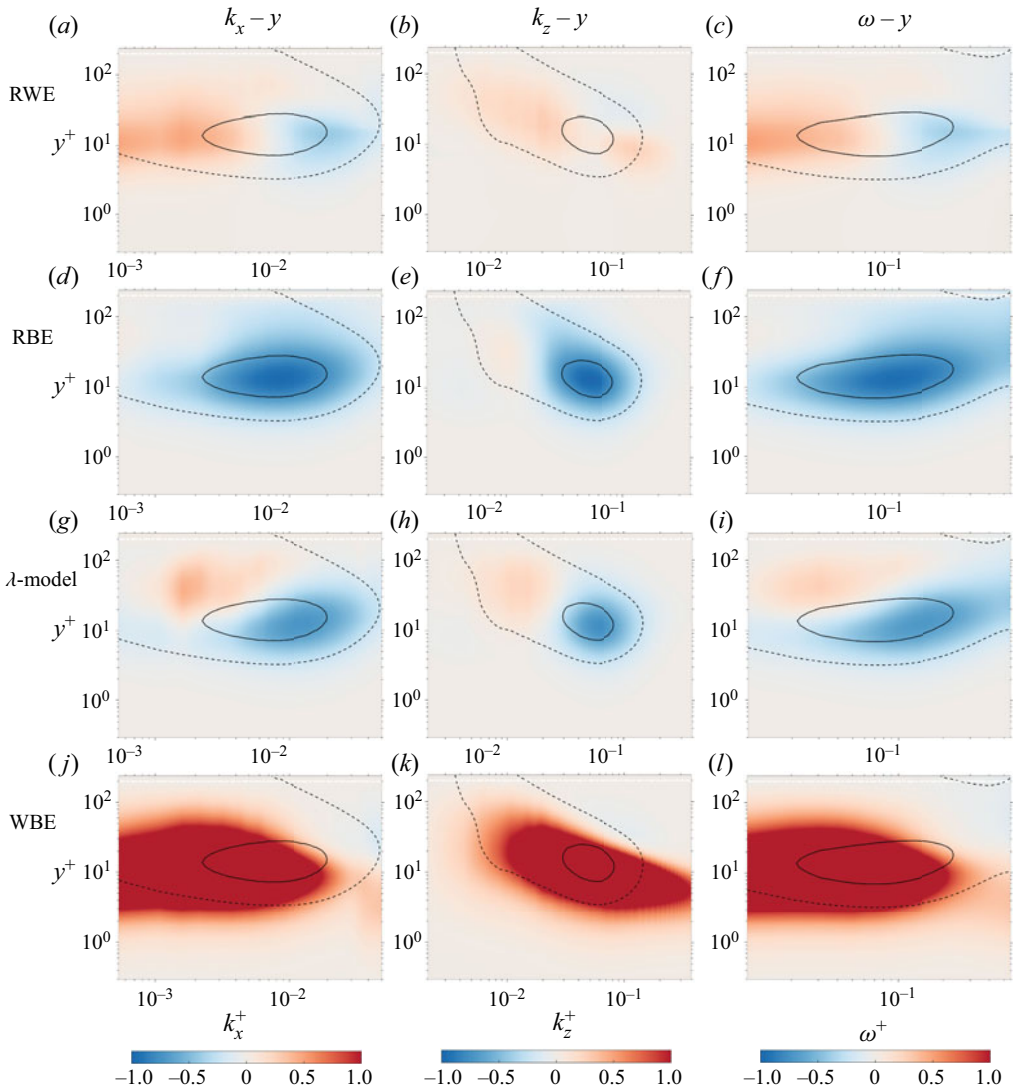


Figure 10. Same as figure 6, but in case 950-200.

4.5. Two-dimensional spectra of the fluctuation velocities

In this section, the two-dimensional auto- and cross-spectra of the fluctuation velocities in the near-wall region ($y^+ = 10$) are analysed to investigate the energy distributions and correlations at different spatial scales. For brevity, the results for the auto-spectra of the streamwise velocity and the cross-spectra of the streamwise and wall-normal velocities are presented for the analyses.

First, the results of streamwise velocity in cases 180-40, 550-100 and 950-200 at the near-wall plane at $y^+ = 10$ are presented in figure 12. In order to show the relative energy spectrum predicted by the WBE, the separate colour bar with its upper bound set as the maximum spectral energy predicted by the WBE is used. Meanwhile, the relative errors of the premultiplied spectra are depicted in figure 13, with the black solid and dashed lines denoting the contours of $0.75S_{DNS,max}$ and $0.25S_{DNS,max}$ of the DNS results, respectively.

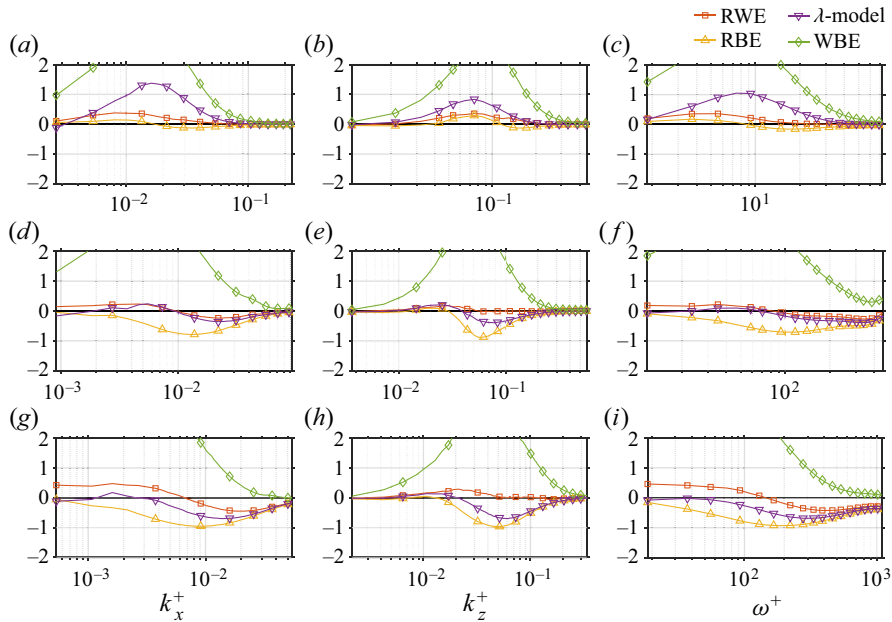


Figure 11. Relative error of the predicted energy at $y^+ = 15$ along k_x^+ (a,d,g), k_z^+ (b,e,h) and ω^+ (c,f,i) in cases 180-40 (a-c), 550-100 (d-f) and 950-200 (g-i). The values of the curves are normalized by $S_{DNS,max}$.

When $Re_\tau = 180$ with $y_R^+ = 40$, it is observed that the predictions of RWE and RBE are relatively consistent with the DNS results. On the other hand, the λ -model and WBE obviously overestimate the spectral energy. This observation is consistent with that in the one-dimensional spectra as discussed in § 4.4. With the increase of the reference height y_R^+ , the predicted energies from the RBE and λ -model decrease correspondingly. When $y_R^+ = 200$, only a small amount of the RBE-predicted energy is observed in the large-scale region with $\lambda_x/h \geq 2$, which indicates that the RBE becomes invalid when the reference layer in this case. In § 4.4, we have observed that the λ -model-predicted one-dimensional energy distributions match well with the DNS results with a wide range of k_x^+ and k_z^+ values. However, when considering the energy distributions as binary functions of λ_x and λ_z , the λ -model results are not consistent with the DNS. From figure 13, the energy predicted by the λ -model is obviously lower than the DNS result, in the energetic region denoted by the black dashed lines. In the RWE results, the energy-concentrating regions that are surrounded by the black dashed lines in figure 12 match well with the DNS results. From figure 13, the largest relative error in the RWE results occurs in case 180-40, which is equal to $0.48S_{DNS,max}$. In cases 550-100 and 950-200, the relative error is always lower than $0.4S_{DNS,max}$. As consistent with the one-dimensional results, the WBE results are overestimated by more than 4 times in magnitude for all the cases. Whereas the WBE results fairly reflect the energy distributions from the DNS.

Then, the cross-spectra between u' and v' at $y^+ = 10$ are investigated, as shown in figure 14 with the relative errors presented in figure 15. The values in figures 14 and 15 are normalized by the peak absolute value of the DNS results, as denoted by $|S_{DNS}|_{max}$ here. The region with large values of negative correlations between the streamwise and wall-normal velocities are observed in each case from the DNS results, which is slightly offset towards smaller flow scales than the auto-spectra as in figure 12. In case 180-40, the RBE provides the most accurate result of the cross-spectra. The RWE

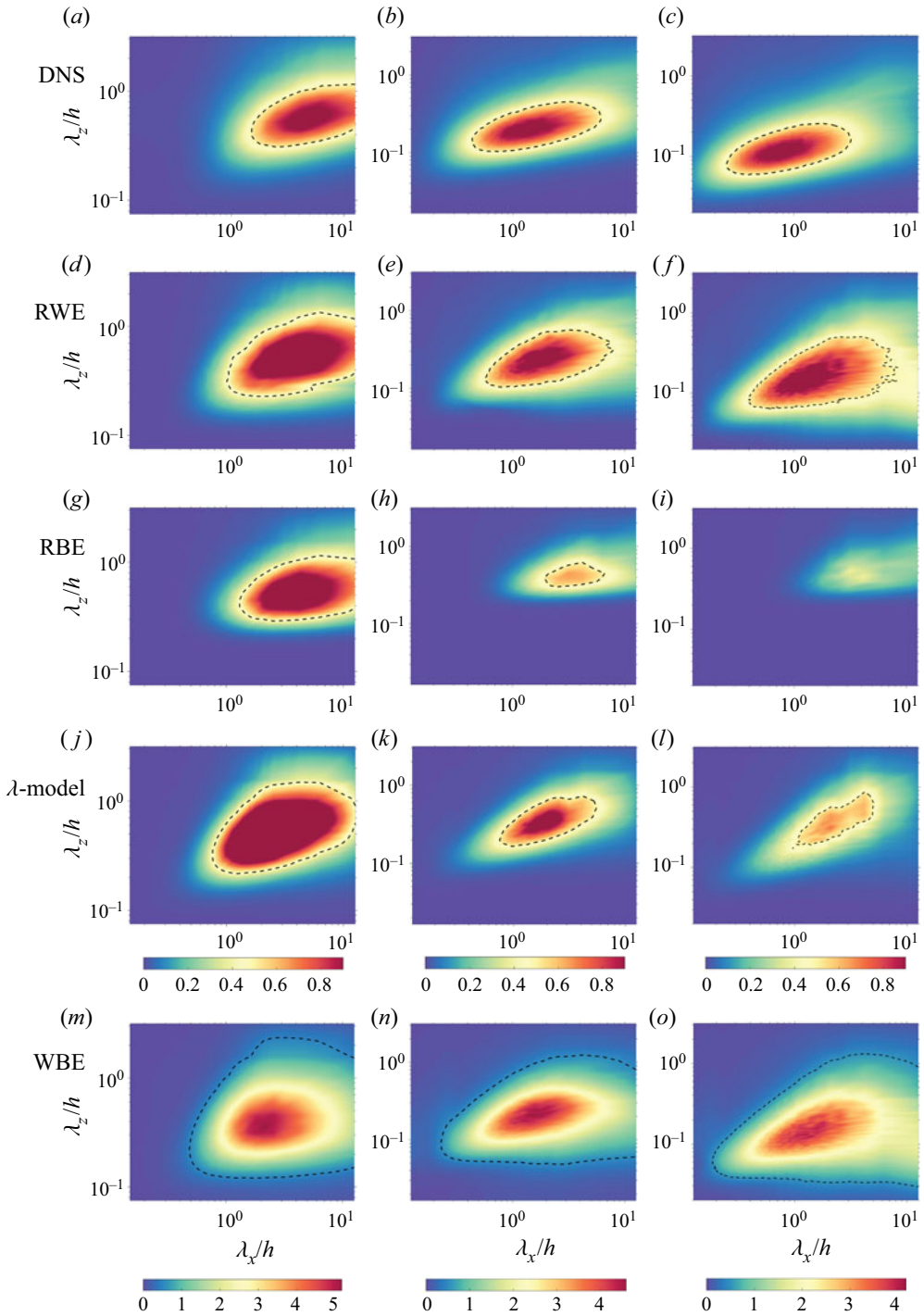


Figure 12. Premultiplied energy spectra as a function of the streamwise wavelength λ_x and spanwise wavelength λ_z from the results of DNS (a–c), RWE (d–f), W-model (g–i), RBE (j–l) and WBE (m–o), at $y^+ = 10$ in case 180-40 (a,d,g,j,m), case 550-100 (b,e,h,k,n) and case 950-200 (c,f,i,l,o). The values shown in the panels are normalized by $S_{DNS,max}$.

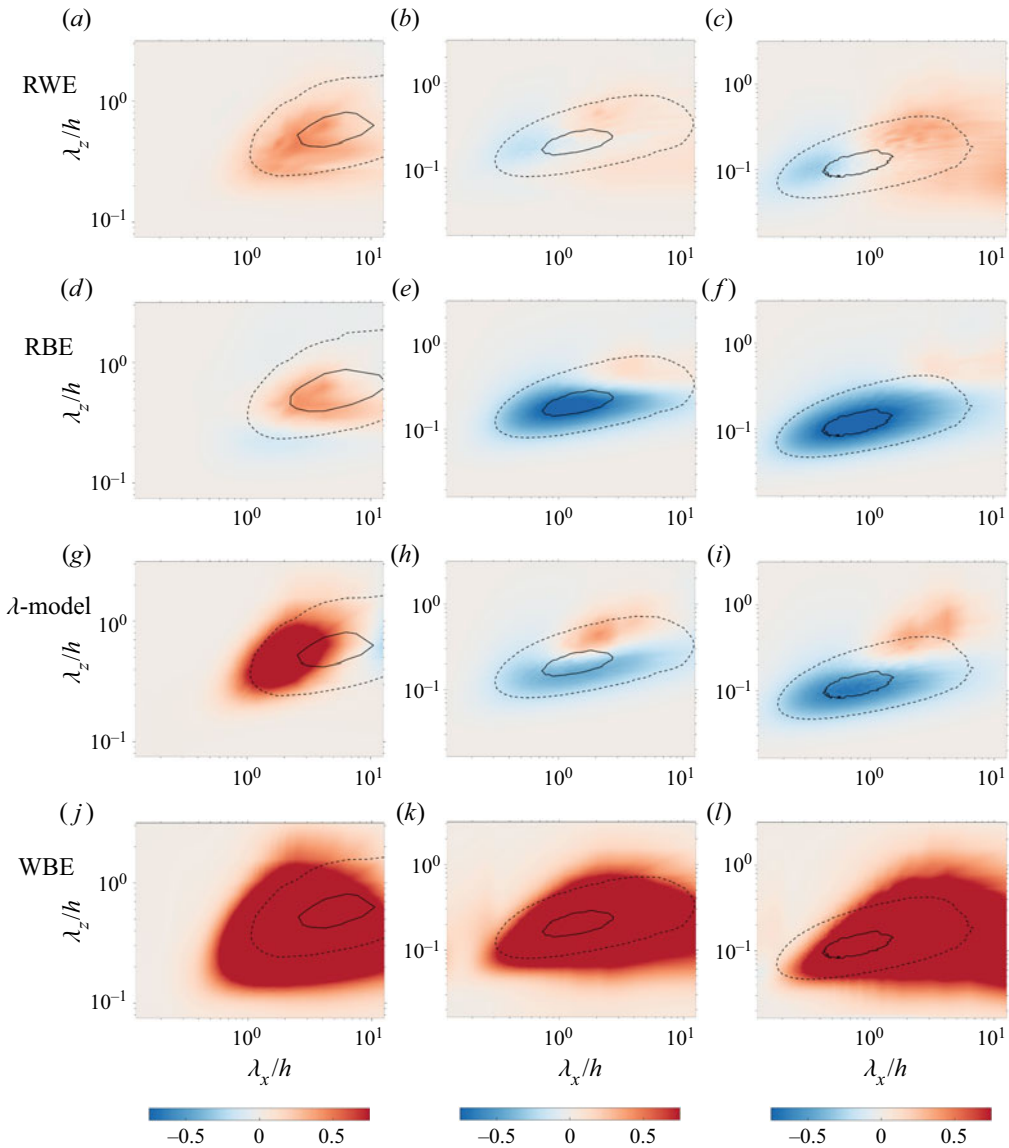


Figure 13. Relative errors of the predicted premultiplied energy spectra normalized by the maximum energy spectra density from DNS as a function of the streamwise wavelength λ_x and spanwise wavelength λ_z from the results of RWE (a–c), W-model (d–f), RBE (g–i) and WBE (j–l), at $y^+ = 10$ in case 180-40 (a,d,g,j), case 550-100 (b,e,h,k) and case 950-200 (c,f,i,l). The values shown in the panels are normalized by $S_{DNS,max}$.

result is larger in magnitude than the DNS results for approximately $0.3|S_{DNS}|_{max}$ in the energy-concentrating region in case 180-40. Meanwhile, the relative errors of the RWE results are much smaller than those in the λ -model and WBE results. As the reference layer lifts up to $y^+ = 100$ and 200 , both the RBE and λ -model obviously underestimate the correlations between u' and v' . Meanwhile, the RWE keeps a relatively low prediction error in the estimation of the cross-spectra in cases 550-100 and 950-200.

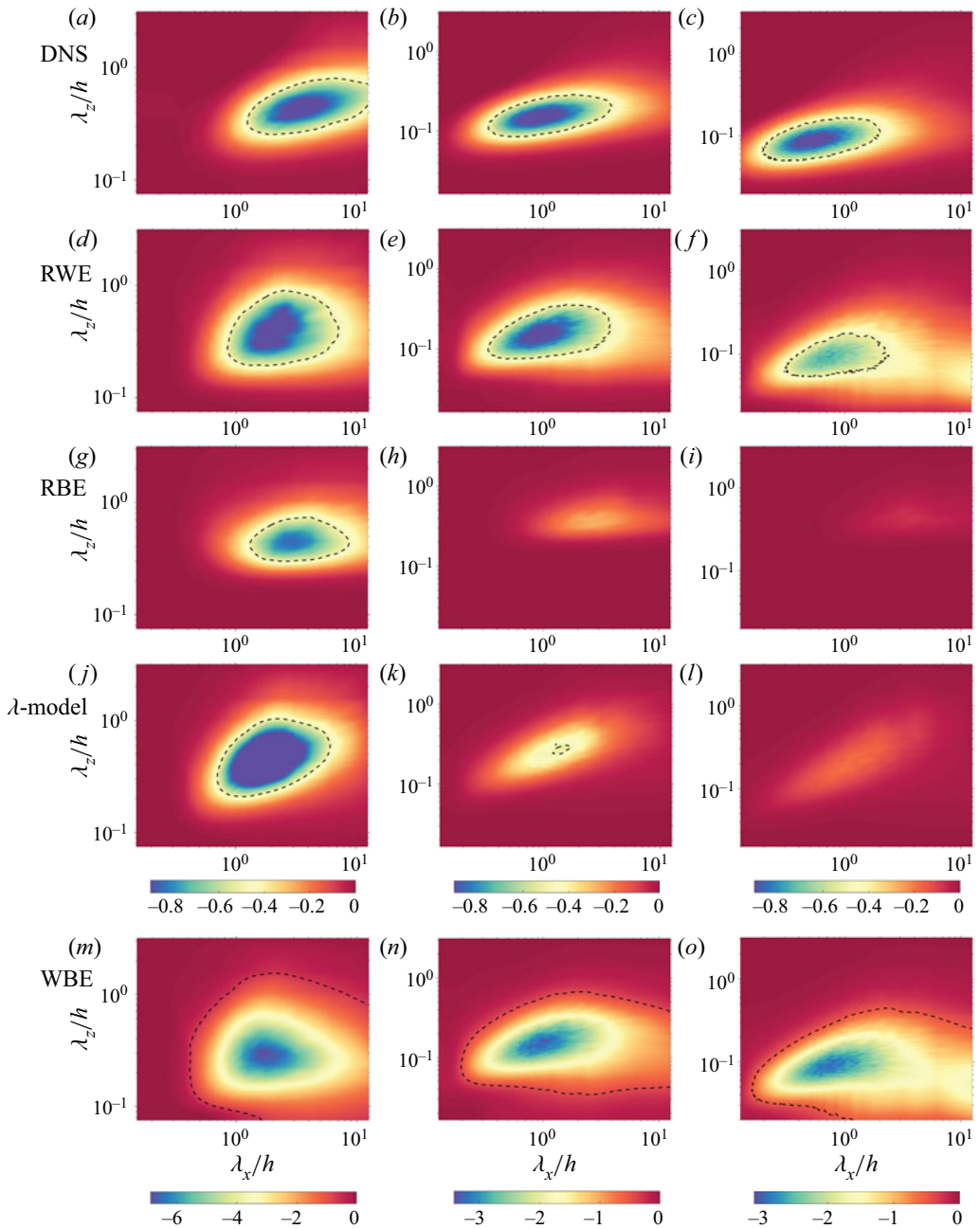


Figure 14. The same as figure 12, but for the premultiplied cross-spectra between u' and v' at $y^+ = 10$. The values shown in the panels are normalized by $|S_{DNS}|_{max}$. Case 180-40 (a,d,g,j,m), case 550-100 (b,e,h,k,n) and case 950-200 (c,f,i,l,o).

4.6. Space-time properties of the fluctuation velocities near the wall

The space-time correlation is an important property of turbulence (He, Jin & Yang 2017). According to Taylor's frozen hypothesis (Taylor 1938), the spatial distributions of the turbulent motions are carried past a fixed point by the convection velocity without significant changes. However, Taylor's frozen hypothesis cannot accurately describe the

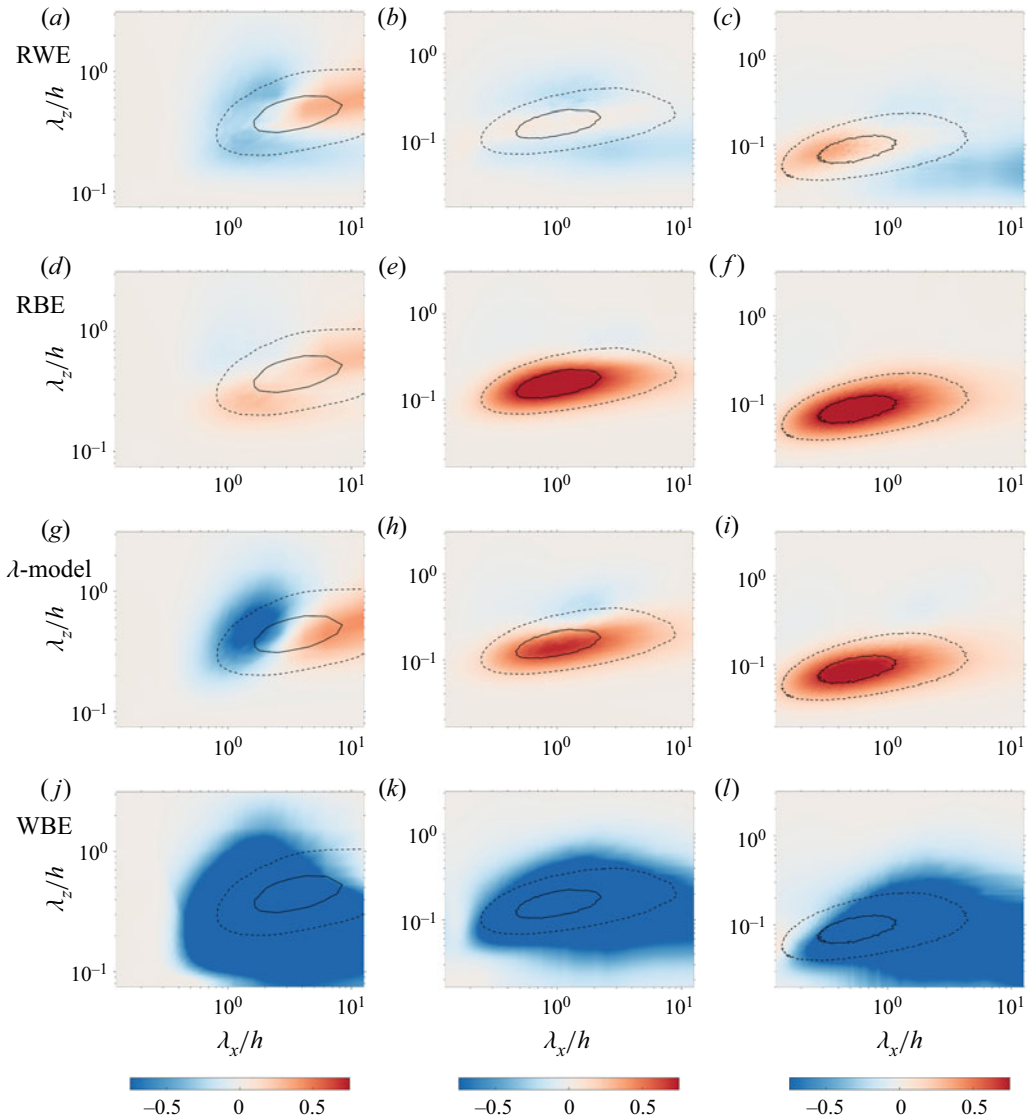


Figure 15. The same as figure 13, but for the relative errors of the premultiplied cross-spectra between u' and v' at $y^+ = 10$. The values shown in the panels are normalized by $|S_{DNS}|_{max}$. Case 180-40 (a,d,g,j), case 550-100 (b,e,h,k) and case 950-200 (c,f,i,l).

complex space–time properties of turbulence (He & Zhang 2006; He *et al.* 2017). In this section, we will test the capability of the newly proposed RWE method in estimating the space–time properties of turbulence in the near-wall region.

The space–time correlation $R(r, \tau)$ is defined as the correlation of the velocity fluctuation at (x, t) and $(x + r, t + \tau)$, which can be calculated by

$$R(r, \tau) = \frac{\langle u'(x, t)u'(x + r, t + \tau) \rangle}{\sqrt{\langle u'(x, t)^2 \rangle \langle u'(x + r, t + \tau)^2 \rangle}} = \frac{\sum_k \mathbf{S}_{uu,k} \exp(i(k_x r - \omega \tau))}{\sum_k \mathbf{S}_{uu,k}}, \quad (4.1)$$

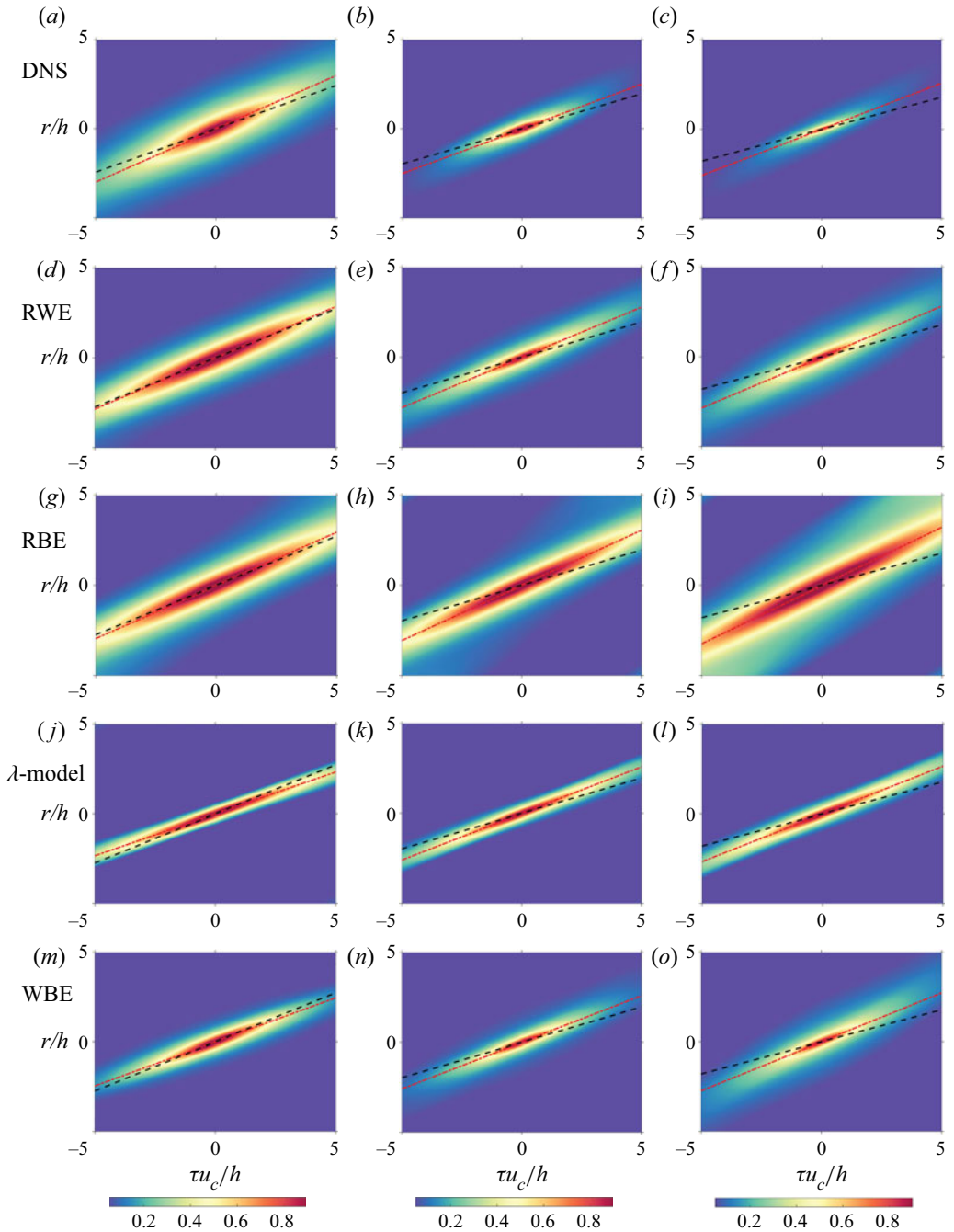


Figure 16. Space-time correlation of the streamwise velocity from the results of DNS (a–c), RWE (d–f), λ -model (g–i), RBE (j–l) and WBE (m–o) at $y^+ = 10$ in cases 180–40 (a,d,g,j,m), 550–100 (b,e,h,k,n) and 950–200 (c,f,i,l,o). The slope of the black dashed lines denotes the mean streamwise velocity at the prediction layers, while the red dot-dashed lines denote the convection velocity calculated by (4.2).

for stationary stochastic processes in the x and temporal direction such as the fully developed turbulent channel flow. With (4.1), the space–time correlation can be estimated using the predicted spectra $\mathbf{S}_{uu,k}$. The space–time correlations of the streamwise velocity obtained from different methods are depicted in figure 16, where the slopes of the black and red dashed lines respectively denote the local mean streamwise velocity $\langle u \rangle$ and the convection velocity U_c , as defined by

$$U_c = \arg \max_U \int_{-\infty}^{\infty} R(Ut, t) dt, \quad (4.2)$$

following Choi & Moin (1990). From the DNS results in figures 16(a)–16(c), the magnitude of the space–time correlation at a given spatio-temporal point increases with the increasing Re_τ , which is due to inner-flow scaling (Kunkel & Marusic 2006) for the flows in the near-wall region. In all three cases, the red dashed line that denotes the convection velocity U_c does not overlap with the black one that denotes the local mean streamwise velocity $\langle u \rangle$, where $U_c > \langle u \rangle$. The deviations of U_c and $\langle u \rangle$ in the near-wall region are consistent with previous observations (Kim & Hussain 1993; Del Alamo & Jiménez 2003). Since the convection velocity U_c quantifies the propagation of the coherent structures (Kim & Hussain 1993; He *et al.* 2017), the near-wall flow structures are propagated with a larger velocity than the local streamwise velocity.

In the predicted results from the four considered methods, quite diverse patterns are observed. In case 180-40, the RWE and RBE results match well with the DNS results in terms of the correlation magnitude. However, the convection velocities predicted by the RWE and RBE are slightly lower than the DNS results, as the slopes of the predicted red dashed lines are smaller than those of the DNS. On the other hand, the space–time correlations predicted by the λ -model and WBE deviate even larger from the DNS results. For the λ -model, the regions where the space–time correlations are larger than 0.2 concentrate at the vicinity of the red dashed line corresponding to the convection velocity, which conflicts with the turbulence nature (He *et al.* 2017). The space–time correlation predicted by the WBE is smaller than that from the DNS at a given spatio-temporal point. Moreover, the convection velocities predicted by the λ -model and WBE appear to be smaller than the local mean streamwise velocity, with relative errors larger than those of the RWE and RBE results in magnitude.

When the reference height y_R increases from 40 to 200, the space–time correlations predicted by RWE tend to become larger compared with the DNS results, which indicates that the large-scale motions are overestimated as the reference layer lifts up. The RBE-predicted results show a much larger overestimation of the space–time correlations, with the dark red region where the correlation magnitude is larger than 0.6 occupying the depicted area when $y_R^+ = 200$. Meanwhile, the convection velocity predicted by the RBE is obviously larger than the DNS results in case 950-200. As discussed in figure 12, only the turbulent motions with large scales with $\lambda_x/h \geq 2$ are estimated by the RBE at $y^+ = 10$ in case 950-200, which means that the space–time correlations predicted by the RBE are dominated by the large-scale flow motions with high spatio-temporal coherence. The λ -model-predicted correlations are large in magnitude in the region close to the red dashed line that denotes the convection velocity, which totally deviates from the patterns of the DNS results. The space–time correlation distributions predicted by the WBE also appear to increase in magnitude as the reference layer lifts up.

From the above discussions on the space–time properties, it is noticed that the predicted near-wall convection velocities are quite different among the results from

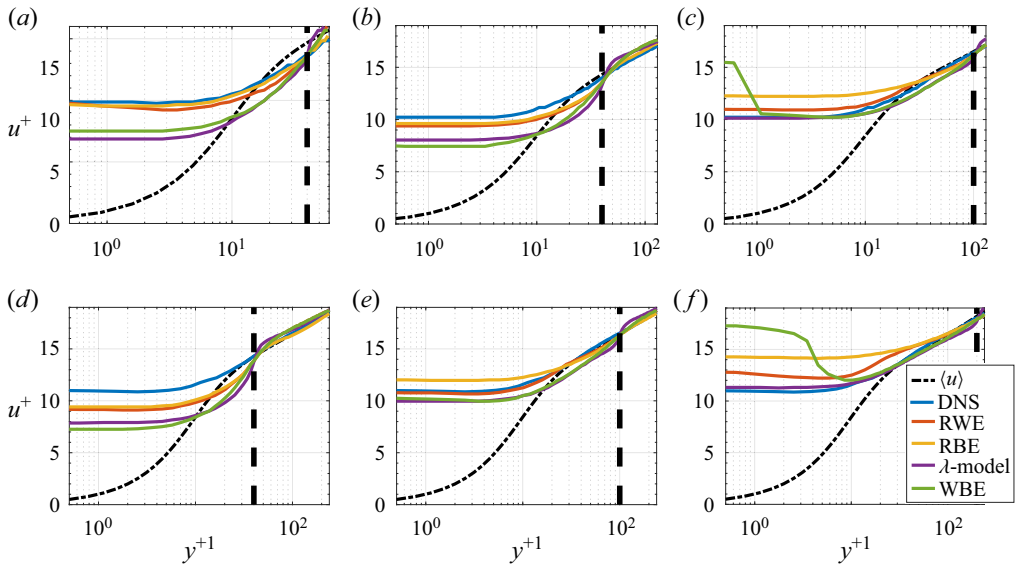


Figure 17. Convection velocity as a function of y^+ for cases 180-40 (a), 550-40 (b), 550-100 (c), 950-40 (d), 950-100 (e) and 950-200 (f).

different methods. To further investigate the variations of the predicted convection velocity with different Reynolds numbers and reference heights, [figure 17](#) shows convection velocity U_c as a function of y^+ in all six cases with $Re_\tau = 180-950$ and the reference layer, ranging from $y^+ = 40$ to $y/h = 0.2$. The relative errors of the predicted convection velocities for different methods along the height are shown in [figure 18](#). Distinct characteristics are observed in the convection velocities predicted by different methods. For RBE, the convection velocity matches well with the DNS results when $y_R^+ = 40$ with all the three considered friction Reynolds numbers that are equal to 180, 550 and 950. In case 950-40, the RBE-predicted convection velocity is lower than the DNS results near the wall by approximately 14 %, which is still the most accurate compared with the results from other prediction methods. With the increase of the reference height, the near-wall convection velocity by RBE increases and thus deviates from the DNS results, which is attributed to the underestimated near-wall small-scale flows with smaller convection velocities compared with those of the large-scale motions. On the other hand, the WBE and λ -model underestimate the convection velocity when $y_R^+ = 40$, which should be induced by the overestimated small-scale flows near the wall. With the increase of reference height, the predicted convection velocities by λ -model and WBE increase correspondingly, just like the phenomenon observed in the RBE results. A non-physical increase of U_c when approaching the wall in the WBE results is observed at the near-wall region in cases 550-100 and 950-200, making the WBE-predicted near-wall convection velocity the largest among all the methods. The λ -model provides the most accurate predictions of the convection velocity in cases 550-100 and 950-200. In all the tested cases, the RWE steadily provides fairly well results in predicting the convection velocity. When $y_R^+ = 40$ and 100, the relative errors between the RWE and the DNS results are less than 15 %. When $y_R^+ = 200$, the RWE-predicted convection velocity shows an enlarged deviation with respect to the DNS results with the maximum error equal to 16.4 % near the wall, which is still smaller than that in the WBE and RBE results.

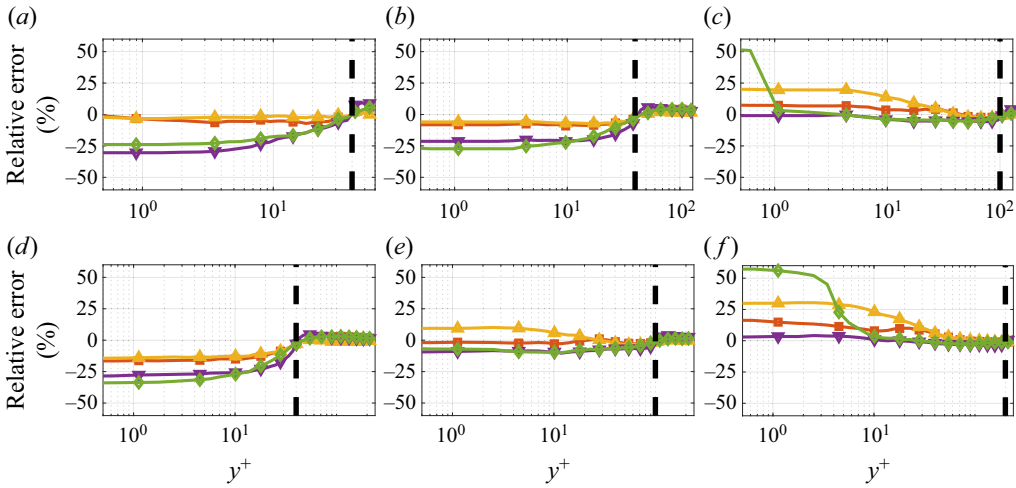


Figure 18. Relative error of the convection velocity as a function of y^+ for cases 180-40 (a), 550-40 (b), 550-100 (c), 950-40 (d), 950-100 (e) and 950-200 (f). The results are plotted in the same colours as those from the same methods in figure 17, respectively.

4.7. Instantaneous large-scale flow structure of the streamwise velocity near the wall

According to the IOIM (Marusic *et al.* 2010; Cheng & Fu 2022), the footprint of the large-scale motions on the lower region can be calculated as

$$u_L^+(x^+, y^+, z^+) = F_x^{-1} \{ H_L(\lambda_x^+, y^+) F_x [u_o^+(x^+, y_o^+, z^+)] \}, \tag{4.3}$$

where u_o^+ is the streamwise velocity fluctuation at y_o^+ in the logarithmic region, and F_x and F_x^{-1} denote the Fourier transform and inverse Fourier transform in the streamwise direction, respectively. Gupta *et al.* (2021) extend the transfer kernel H_L to quantify the correlation between $u^+(y^+)$ and $u_o^+(y_o^+)$ at a given two-dimensional length scale of $(\lambda_x^+, \lambda_z^+)$ rather than just the streamwise scale λ_x^+ . The re-defined transfer kernel H_L can be calculated as

$$\begin{aligned} H_L(\lambda_x^+, \lambda_z^+, y^+) &= \frac{\langle \hat{u}(\lambda_x^+, \lambda_z^+, y^+, z^+) \bar{\hat{u}}(\lambda_x^+, \lambda_z^+, y_o^+, z^+) \rangle}{\langle \hat{u}(\lambda_x^+, \lambda_z^+, y_o^+, z^+) \bar{\hat{u}}(\lambda_x^+, \lambda_z^+, y_o^+, z^+) \rangle} = \frac{S_{uu, y_o y_o}(k_x, k_z)}{S_{uu, y_o y_o}(k_x, k_z)} \\ &= \frac{\sum_{\omega} S_{uu, y_o}(k_x, k_z, \omega)}{\sum_{\omega} S_{uu, y_o y_o}(k_x, k_z, \omega)}. \end{aligned} \tag{4.4}$$

Since all the tested methods can directly predict the CSD tensor of the velocity from the measurements, the transfer kernel H_L can be estimated from the auto-spectrum coefficient $S_{uu, y_o y_o}(k_x, k_z, \omega)$ and the cross-spectrum coefficient $S_{uu, y_o}(k_x, k_z, \omega)$ from the estimated CSD tensor. In Gupta *et al.* (2021), the large-scale fluctuations are estimated with the linear model as in (4.3). Following Gupta *et al.* (2021), we will also conduct the estimation of large-scale structures using the transfer function estimated from the tested methods. Case 950-200, where the reference layer is the farthest away from the wall among all the tested cases, will be used to investigate the estimated footprint at two prediction heights of $y^+ = 100$ and 10 that correspond to the logarithmic region and the near-wall region, respectively.

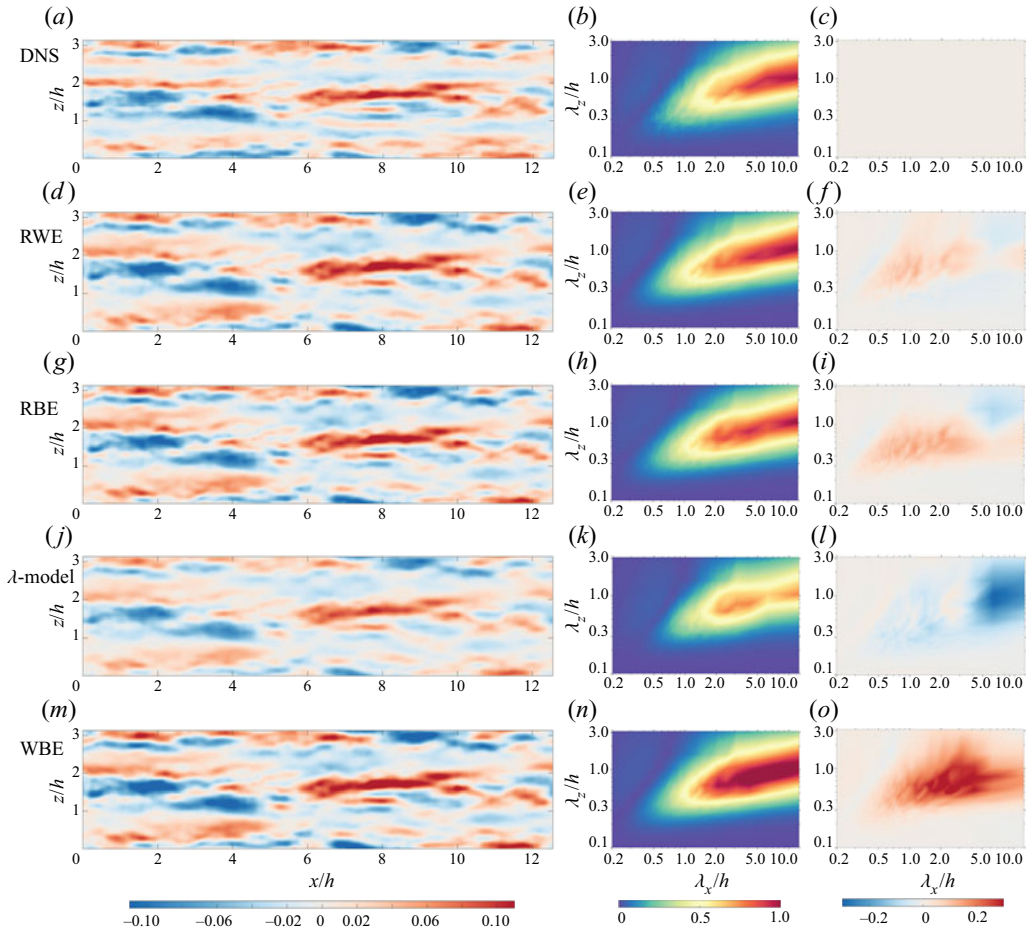


Figure 19. Comparisons of the predicted footprint of the large-scale motions of $y_R^+ = 200$ with the prediction layer of $y^+ = 100$ in case 950-200 from DNS (a–c), RWE (d–f), W-model (g–i), RBE (j–l) and WBE (m–o). Panels (a,d,g,j,m) are the instantaneous flow field, (b,e,h,k,n) are the energy spectra and (c,f,i,l,o) are the relative error normalized by the maximum spectral energy in the DNS results. The values of fluctuation velocity shown in (a,d,g,j,m) are normalized by the mean velocity at $y = h$. The value of spectral energy and relative error shown in (b,e,h,k,n) and (c,f,i,l,o) are normalized by $S_{DNS,max}$, respectively.

Figure 19 shows the estimated large-scale structures of the streamwise velocity fluctuation at $y^+ = 100$. From the instantaneous flow field shown in the left column, the RWE and RBE predictions well reflect the characteristics of the instantaneous flow structures. The good performance of RWE and RBE can also be seen in the spectral space, where the relative errors are smaller compared with those of the λ -model and WBE. Specifically, the relative errors in the RWE results are smaller than those in the RBE results, with a maximum error of $0.13S_{DNS,max}$ in the premultiplied energy spectra. On the other hand, the WBE and λ -model overestimate and underestimate the fluctuation energy at $y^+ = 100$, respectively.

As the prediction layer approaches the wall, the magnitude of relative errors between the predictions from all the tested methods becomes larger, as in figure 20. For the RWE methods, the largest magnitude of error equal to $0.26S_{DNS,max}$ appears at $y^+ = 10$ for the large-scale motions with $(\lambda_x/h, \lambda_z/h) = (6.2, 1.6)$, where the predicted energy is lower than the DNS result. Meanwhile, another extreme point for error from RWE is found

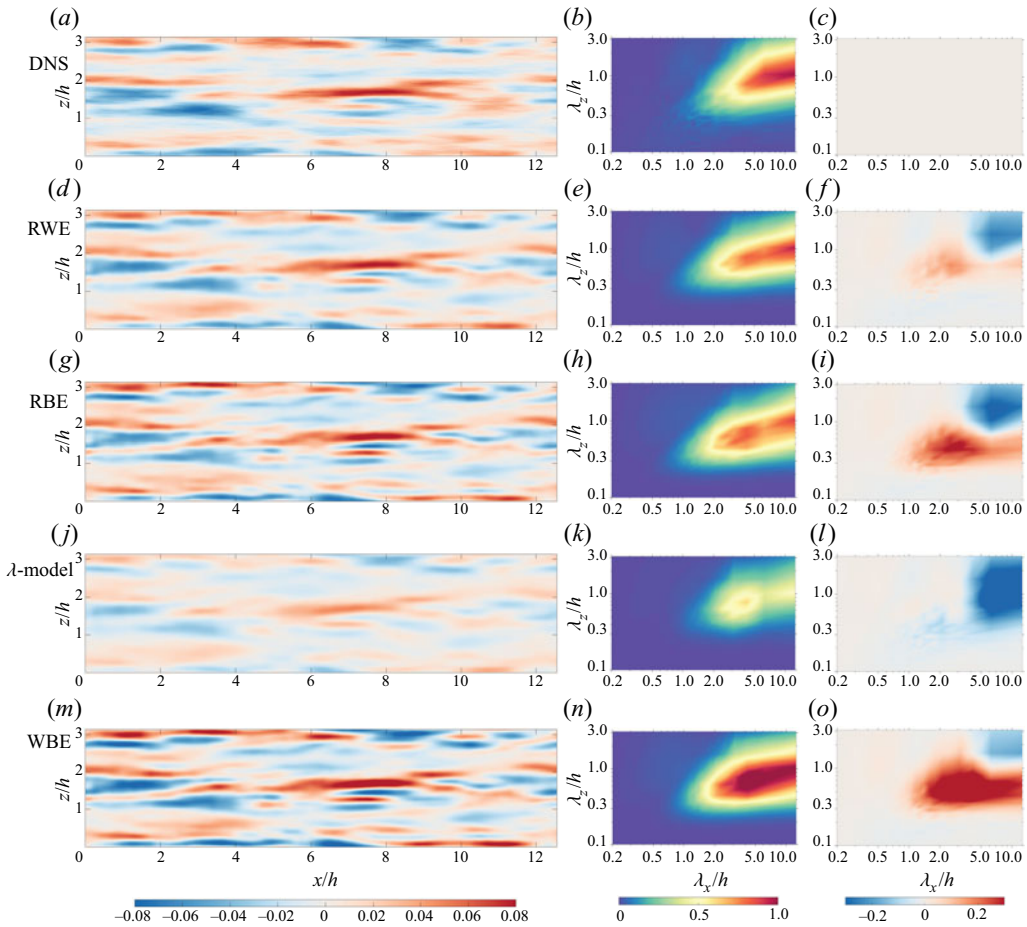


Figure 20. Same as figure 19, but with the prediction layer at $y^+ = 10$.

at $(\lambda_x/h, \lambda_z/h) = (2.5, 0.6)$ with the positive value equal to $0.17S_{DNS,max}$. The relative errors in the RBE predictions reach the extreme points at $(\lambda_x/h, \lambda_z/h) = (6.2, 1.6)$ and $(2.5, 0.4)$. At the extreme points, the errors from RBE are equal to $-0.34S_{DNS,max}$ and $0.32S_{DNS,max}$, both of which are larger than those from RWE at the same points. The λ -model-predicted energy is lower than the DNS for the scales with $\lambda_x/h \geq 6$, with the relative error larger than $0.5S_{DNS,max}$, which indicates that the fluctuation energy predicted by the λ -model is much overestimated in the near-wall region. As for the WBE, the relative error is larger than $0.3S_{DNS,max}$ when $\lambda_x/h \geq 1.8$ and $0.4 \leq \lambda_z/h \leq 0.8$. Considering the above comparisons, the RWE performs better than the other tested methods, with the smallest relative error in the estimated energy spectra at both the logarithmic region and the near-wall region.

In Gupta *et al.* (2021), the λ -model and WBE (namely B-model) are also used to predict the large-scale motions in the near-wall region, with the assumption that the input forcing is white in time, which leads to the same conclusion that the energy predicted by the λ -model is lower than that from the WBE. However, when applied in time-resolved cases as in this study, the energies predicted by the λ -model and WBE both tend to decrease compared with those using the white-in-time forcing in Gupta *et al.* (2021), which causes the obvious underestimation of energy by the λ -model. The deviations between the results

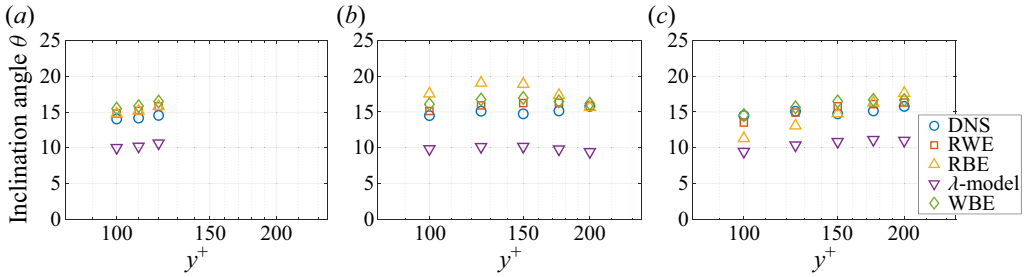


Figure 21. Structure inclination angles of the predicted fluctuation velocity in (a) case 550-100, (b) case 950-100 and (c) case 950-200.

generated by the forcing with different temporal properties indicate that the λ -model could be improved by considering the effect of temporal scales when applied in the time-resolved cases. On the other hand, the validity of the RWE-kind method for estimating large-scale motions in cases where only the spatial data are available should be further tested.

From the instantaneous flow field for large-scale motions as discussed above, the structures are observed to delay backward as the prediction layer approaches the wall. The spatial delay of the flow structure is quantified by the SIA (Marusic & Heuer 2007), which is defined as

$$\theta = \arctan [y/(\Delta x^*)], \tag{4.5}$$

where $\Delta x^* = \arg \max_{\Delta x} R_{\tau u}(\Delta x)$, and

$$R_{\tau u}(\Delta x) = \frac{\langle \tau(t) u(t + \Delta x/U) \rangle}{\sqrt{\langle \tau^2 \rangle \langle u^2 \rangle}} = \frac{\sum_k S_{\tau u, k} \exp(ik_x \Delta x)}{\sigma_\tau \sigma_u}, \tag{4.6}$$

is the correlation function between the wall shear stress and the streamwise velocity fluctuation with a spatial delay of Δx , and $S_{\tau u, k}$ is the cross-spectra between the wall shear and the velocity fluctuations at k . To further investigate the ability of the tested methods in predicting the spatial distribution of the flow structures, the structural inclination angles (SIAs) from the predictions are analysed in the following. Since the logarithmic region does not exist clearly for the channel flow with $Re_\tau = 180$, only the cases 550-100, 950-100 and 950-200 will be discussed.

Figure 21 depicts the SIAs in the tested cases based on the reference positions located inside the logarithmic region from $y^+ = 100$ to $y/h = 0.2$ (Jiménez 2018). According to the DNS results, the inclination angles keep almost constant around 15° at reference positions with different heights, which is consistent with the results in Marusic & Heuer (2007). In case 550-100, all the tested methods fairly predict the inclination angle of around 15° except for the λ -model. In fact, the λ -model-predicted SIAs are always around 10° in all the three cases shown in figure 21. In case 950-100, the RBE-predicted SIA is larger than the DNS result by approximately 3° when $y^+ = 100$. As the height lifts up, the SIA predicted by RBE reaches the maximum value of approximately 19° when $y_R^+ = 125$, then gradually decreases and finally overlaps with the DNS results when $y_R^+ = 200$. The RWE and WBE perform well in case 950-100, with the r.m.s. error compared with the DNS result equal to 0.96° and 1.55° , respectively. When the reference layer moves to $y^+ = 200$, as in figure 21(c), the RBE-predicted SIA is accurate when $y^+ \geq 175$. However, when the horizontal layers approach the wall, the SIA predicted by the RBE decreases, which becomes around 12° when $y^+ = 100$. On the other hand, the RWE has the highest

accuracy, with the root-mean-squared error equal to 0.81° . Meanwhile, the WBE-predicted results are also close to the DNS results, whose r.m.s. error is 1.14° .

Based on the above analyses of the flow structures predicted by the tested methods, the RWE has the best performance in estimating both spectral energy distributions and the structural inclination angles of the large-scale motions of the turbulent channel flow. Meanwhile, the WBE also performs well in predicting the SIAs, indicating that the relative distribution of the coherent structures can be fairly estimated by the WBE which just utilizes the white-noise-assumed forcing.

5. Conclusions

In this study, a new method for predicting the turbulent channel flow is proposed, which is denoted as RWE. The RWE modifies the spatially uniform and uncorrelated forcing profile based on the relative value of response energy in the near-wall region estimated by the RBE (Towne *et al.* 2020). Comprehensive validations are made to investigate the ability of RWE to predict the spectra of the incompressible turbulent channel flow. Time-resolved DNS datasets with $Re_\tau = 180, 550, \text{ and } 950$ are used to provide limited layers of reference measurements for the predictions. The DNS results are further used as a standard to evaluate the accuracy of different prediction methods, including the RWE, λ -model (Gupta *et al.* 2021), RBE and the method using the WBE. To test the sensitivity of the prediction methods on the locations of measurements and the friction Reynolds numbers, several reference layers ranging from $y^+ = 40$ at the near-wall region to $y/h \approx 0.2$ at the upper bound of the logarithmic region are set in cases with $Re_\tau = 180, 550 \text{ and } 950$, resulting in a total number of six cases for the validations.

The r.m.s. profiles of the velocity fluctuations are first tested for all six cases. The r.m.s. profiles predicted by the RWE are pretty consistent with the DNS results. Specifically, the relative deviations of the streamwise r.m.s. peaks between the RWE and DNS results are less than 11 % in all the tested cases, indicating that this newly proposed method is robust in the friction Reynolds numbers and the measurement locations. On the other hand, the performances of the RBE and λ -model show a dependence on the specific measurement locations. The prediction accuracy of RBE is close to that of RWE when the reference layer is located at $y^+ = 40$ that is in the vicinity of the wall. With the increase of the reference height, the accuracy of RBE near the wall deteriorates rapidly. The near-wall energy predicted by the λ -model also decreases when the reference layer lifts. The λ -model reaches its best performance with the reference layer at $y^+ = 100$, and overestimates and underestimates the near-wall energy when $y^+ = 40$ and 200, respectively. In all the tested cases, the WBE largely overestimates the near-wall energy, indicating that the WBE is not suitable to be directly used for the estimations of near-wall energy magnitude.

The prediction capability of the considered methods is further investigated by examining the energy spectra. The RBE continuously shows a good prediction capacity at specific reference layers at $y^+ = 40$. Meanwhile, it is observed that the relative spectra predicted by the WBE can fairly reflect the energy distribution of the DNS results. Compared with the other tested methods, the RWE better predicts the energy distribution of velocity fluctuations at different scales along the heights ranging from the wall to the reference layer. On the other hand, compared with the DNS results, the predicted energy of all the considered methods tends to decrease as the flow scale decreases, while the RWE keeps the minimum relative error.

The space–time properties of the predicted flow field are also investigated, including the magnitude of the space–time correlation and the convection velocity. In case 950-200, the magnitude of space–time correlations is overestimated by all the methods, while the

RWE and WBE provide the closest results compared with the DNS. On the other hand, the RBE obviously overestimates the correlation magnitude, especially at the near-wall region $y^+ = 10$ due to the underestimation of the small-scale motions. The convection velocity of the coherent structures is also studied. The RBE and RWE results match well with the DNS when the reference layer is located at $y^+ = 40$ that is close to the wall. However, the predicted convection velocity in the near-wall region by the RBE and RWE increases with the increasing height of the reference layer, which reaches the maximum error when $y^+ = 200$. In case 950-200, the RWE-predicted convection velocity is larger than the DNS result by 16.4 % at the near-wall region, which is smaller than the WBE and RBE.

The instantaneous flow field near the wall can be predicted based on the estimated CSD sensor and the reference velocity signal in the logarithmic region. The large-scale structures are well predicted by the RWE and RBE. On the other hand, the λ -model and WBE underestimate and overestimate the energies of the near-wall large-scale motions, respectively. The SIAs from the tested methods are researched to further investigate the characteristics of the predicted flow structures. The WBE and RWE perform well in predicting the SIAs in cases 550-100 and 950-200 when compared with the DNS results, i.e. at around 15° .

From the above discussions, the strategy to modify the forcing profile informed by the RBE shows a strong potential in predicting the turbulent statistics of incompressible channel flows. Meanwhile, there are some discussions on the application scope of the current RWE method and its future extensions. (i) In this study, we focus on estimating the near-wall statistics based on the measurements in the higher region, especially for the cases where the reference layer is located in the logarithmic region. A related problem could be the estimation of the flow patterns in the logarithmic region based on the wall measurements, which is explored by Amaral *et al.* (2021) using the RBE and Guastoni *et al.* (2021) using the CNN. Due to the restrictions of $y_Q \leq y_R$ when determining the quasi-reference layer, the current RWE will degenerate to WBE when $y_R \rightarrow 0$. To effectively make use of the wall measurements, the way to determine y_Q in the current RWE should be modified, which can be explored in future studies. (ii) The current RWE approach only uses one type of observation at one reference layer. It is clear that the prediction accuracy could be further improved with different measurements at multiple reference layers with suitable modelling approaches. Such a topic is to be explored in the future work. (iii) The method used in this study relies on the availability of time-resolved measurement data. The RWE could be more practical if it can predict the flow with measurement data that are sparse in time, which might be realized using the assumptions of the stochastic forcing as used by Hwang & Cossu (2010) and Gupta *et al.* (2021). (iv) Possible extensions of the RWE to other types of turbulent flows, such as the pipe flows, boundary layers and jet flows, could be explored in the future. For wall-bounded turbulence, the basic steps of the RWE can be directly applied. According to Monty *et al.* (2009) and Lee & Sung (2013), the differences between the channel/pipe flows and boundary layers are obvious in the very-large-scale motions, which are energetic in the outer region. In the inner region where the RWE is applied, the differences in flow structures are not as obvious as those in the outer region. Thus, the RWE is believed to be valid in estimating the wall-bounded turbulence, including the turbulent pipe flows and boundary layers. For jets, the approach of RWE developed in this study could not be directly applied, since the flow pattern is different from that of the wall-bounded turbulence. In Schmidt *et al.* (2018), the inclusion of the eddy viscosity has been demonstrated to largely improve the agreement with the resolvent modes and the spectral proper orthogonal decomposition modes, which implies the potential of linear estimation

of jets in the future. However, to our knowledge, the applicability of the RBE for jets from limited measurements is not fully investigated. Future studies are needed to explore the applications of the RWE-like methods in estimating the jets. (v) The validity of the RWE in predicting the compressible or stratified turbulence has not been tested, which should be comprehensively investigated in the future.

Funding. L.F. acknowledges the fund from the Research Grants Council (RGC) of the Government of Hong Kong Special Administrative Region (HKSAR) with RGC/ECS Project (no. 26200222) and RGC/GRF Project (no. 16201023), the fund from CORE as a joint research centre for ocean research between QNLM and HKUST, and the fund from the Project of Hetao Shenzhen-Hong Kong Science and Technology Innovation Cooperation Zone (no. HZQB-KCZYB-2020083). This work is also partially supported by the Research Grants Council (RGC) of the Government of Hong Kong Special Administrative Region (HKSAR) with RGC/STG Project (no. STG2/E-605/23-N).

Declaration of interests. The authors report no conflict of interest.

Data availability. The data that support the findings of this study are available on request from the corresponding author, L.F.

Author ORCIDs.

-  Anjia Ying <https://orcid.org/0000-0002-3358-2786>;
-  Tian Liang <https://orcid.org/0000-0002-6299-7294>;
-  Zhigang Li <https://orcid.org/0000-0001-7164-1049>;
-  Lin Fu <https://orcid.org/0000-0001-8979-8415>.

Appendix A. Linearized Navier–Stokes operator

Recall the discretized state-space form of the linearized Navier–Stokes equations as

$$\mathbf{M} \frac{\partial \mathbf{q}_{k_s}(t)}{\partial t} = \mathbf{A}_{k_s} \mathbf{q}_{k_s}(t) + \mathbf{B} \mathbf{f}_{k_s}(t), \tag{A1a}$$

$$\mathbf{m}_{k_s}(t) = \mathbf{C} \mathbf{q}_{k_s}(t) + \mathbf{n}_{k_s}(t). \tag{A1b}$$

The operators $\mathbf{M} \in \mathbb{C}^{4N \times 4N}$, $\mathbf{A}_{k_s} \in \mathbb{C}^{4N \times 4N}$, $\mathbf{B} \in \mathbb{C}^{4N \times 3N}$ in (A1a) are expressed as

$$\mathbf{M} = \begin{bmatrix} \mathbf{I}_N & 0 & 0 & 0 \\ 0 & \mathbf{I}_N & 0 & 0 \\ 0 & 0 & \mathbf{I}_N & 0 \\ 0 & 0 & 0 & 0 \end{bmatrix}, \quad \mathbf{A}_{k_s} = \begin{bmatrix} \mathbf{L}_{k_s} & -\nabla^T \\ \nabla & 0 \end{bmatrix}, \quad \mathbf{B} = \begin{bmatrix} \mathbf{I}_N & 0 & 0 \\ 0 & \mathbf{I}_N & 0 \\ 0 & 0 & \mathbf{I}_N \\ 0 & 0 & 0 \end{bmatrix}. \tag{A2a-c}$$

The spatial linearized Navier–Stokes operator $\mathbf{L}_{k_s} \in \mathbb{C}^{3N \times 3N}$ in (A2a-c) for the momentum equations is calculated as

$$\mathbf{L}_{k_s} = \mathbf{L}_0 + ik_x \mathbf{L}_x + \mathbf{L}_y \mathbf{D} + ik_z \mathbf{L}_z + \mathbf{L}_2 (-k_x^2 \mathbf{I} + \mathbf{D}^2 - k_z^2 \mathbf{I}), \tag{A3}$$

with

$$\left. \begin{aligned} \mathbf{L}_x &= \begin{bmatrix} \bar{\mathbf{u}} & -\mathbf{v}'_T & 0 \\ 0 & \bar{\mathbf{u}} & 0 \\ 0 & 0 & \bar{\mathbf{u}} \end{bmatrix}, \quad \mathbf{L}_y = \begin{bmatrix} -\mathbf{v}'_T & 0 & 0 \\ 0 & -2\mathbf{v}'_T & 0 \\ 0 & 0 & -\mathbf{v}'_T \end{bmatrix}, \quad \mathbf{L}_z = \begin{bmatrix} 0 & 0 & 0 \\ 0 & 0 & 0 \\ -\mathbf{v}'_T & 0 & 0 \end{bmatrix}, \\ \mathbf{L}_0 &= \begin{bmatrix} 0 & \mathbf{u}' & 0 \\ 0 & 0 & 0 \\ 0 & 0 & 0 \end{bmatrix}, \quad \mathbf{L}_2 = \begin{bmatrix} -\mathbf{v}_T & 0 & 0 \\ 0 & -\mathbf{v}_T & 0 \\ 0 & 0 & -\mathbf{v}_T \end{bmatrix}, \end{aligned} \right\} \tag{A4}$$

where $\bar{\mathbf{u}} = \text{diag}[\bar{u}_1]$, \bar{u}_1 is the mean streamwise velocity profile, $\mathbf{v}_T = (1/Re_\tau)\text{diag}[(1/\nu)v_T]$, $\mathbf{v}'_T = (1/Re_\tau)\text{diag}[(1/\nu)v'_T]$, \mathbf{D} and $'$ denote $\partial/\partial y$. The Hamiltonian operator $\nabla \in \mathbb{C}^{N \times 3N}$ in (2.7) is calculated as

$$\nabla = [ik_x I_N \quad \mathbf{D} \quad ik_z I_N]. \tag{A5}$$

The observation matrix \mathcal{C} in (A1b) is determined by the location of the measured variable. In this study, the state matrix is assembled as

$$\mathbf{q}_{k_s}(t) = [\mathbf{u}_{k_s}^T(t), p_{k_s}(t)]^T = [u_{k_s}(t), v_{k_s}(t), w_{k_s}(t), p_{k_s}(t)]^T. \tag{A6}$$

Denoting $(u_1, u_2, u_3) = (u, v, w)$, when the measured variable is the velocity u_i ($i = 1, 2, 3$) at the n th node, then the observation matrix $\mathcal{C} \in \mathbb{C}^{1 \times 4N}$ should be expressed as

$$\mathcal{C} = [\mathbf{O}_{1 \times [(i-1)N+n-1]} \quad 1 \quad \mathbf{O}_{1 \times [4N-(i-1)N-n]}]. \tag{A7}$$

Note that, in other cases, such as when the state matrix is assembled in another approach or the measurements are located at multiple wall-normal locations, the expression of the measurement operator should be redetermined in an analogous manner. For instance, in (2.15), the resolvent operator \mathbf{R}_k is utilized, which excludes the rows corresponding to the pressure state. In this case, when the measured variable is the velocity u_i ($i = 1, 2, 3$) at the n th node, the observation matrix as denoted by \mathcal{C} should be calculated by

$$\mathcal{C} = [\mathbf{O}_{1 \times [(i-1)N+n-1]} \quad 1 \quad \mathbf{O}_{1 \times [3N-(i-1)N-n]}]. \tag{A8}$$

Appendix B. Assessment of the DNS dataset generated in this study

In figure 22, the DNS dataset generated in this study is compared with the open source DNS database (Del Alamo & Jiménez 2003; Hoyas & Jiménez 2008) for the mean streamwise velocity and the r.m.s. velocities. Very small differences are found between the two datasets, which demonstrates that the DNS data generated in this study are reliable.

Appendix C. Discussions on the determination of quasi-reference layer

The LCS (γ^2) used to determine the quasi-reference layer y_Q is estimated using the WBE in each spatio-temporal scale. This quantity is obtained by firstly estimating the CSD tensor with the white-noise-assumed forcing through (2.12), i.e.

$$\mathbf{S}_{uu,k} = \mathbf{R}_k \mathbf{S}_{ff,k} \mathbf{R}_k^* = E_k \mathbf{R}_k \mathbf{R}_k^*. \tag{C1}$$

From the definition of γ^2 in (3.2), and considering (C1), γ^2 is calculated by

$$\begin{aligned} \gamma^2(\mathbf{k}) &= \frac{\left| \langle \hat{u}(y_Q^+) \overline{\hat{u}(y_P^+)} \rangle \right|^2}{\left\langle \left| \hat{u}(y_Q^+) \right|^2 \right\rangle \left\langle \left| \hat{u}(y_P^+) \right|^2 \right\rangle} \\ &= \frac{\mathbf{S}_{uu,k}^2(y_Q^+, y_P^+)}{\mathbf{S}_{uu,k}(y_Q^+, y_Q^+) \mathbf{S}_{uu,k}(y_P^+, y_P^+)} \\ &= \frac{\left| \mathcal{C}(u, y_Q^+) \mathbf{R}_k \mathbf{R}_k^* \mathcal{C}^T(u, y_P^+) \right|^2}{\left[\mathcal{C}(u, y_Q^+) \mathbf{R}_k \mathbf{R}_k^* \mathcal{C}^T(u, y_Q^+) \right] \cdot \left[\mathcal{C}(u, y_P^+) \mathbf{R}_k \mathbf{R}_k^* \mathcal{C}^T(u, y_P^+) \right]}, \end{aligned} \tag{C2}$$

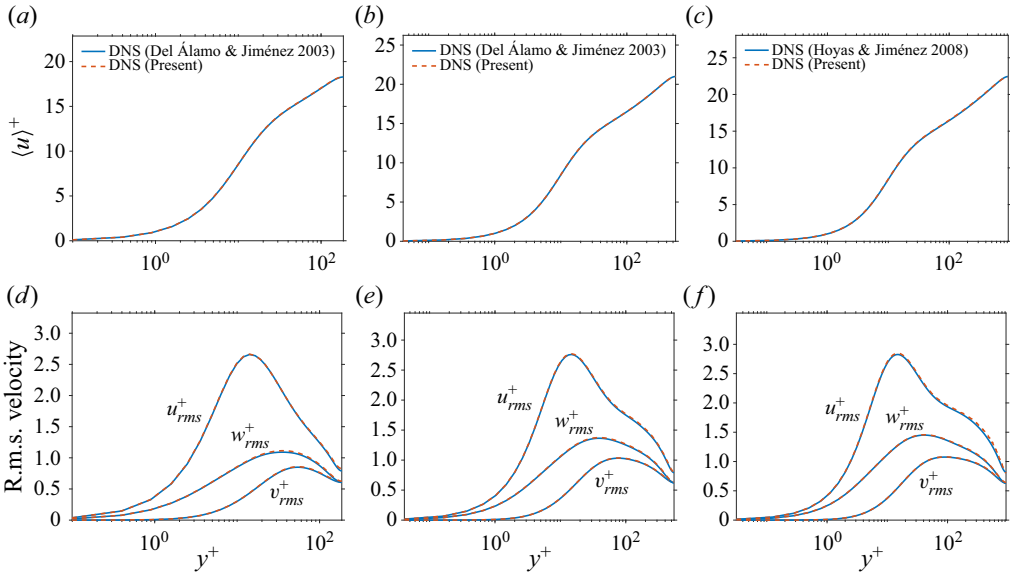


Figure 22. Comparisons of the mean and r.m.s. profiles between the open-source DNS results (Del Álamo & Jiménez 2003; Hoyas & Jiménez 2008) and those generated in this study; (a,d) $Re_\tau = 180$, (b,e) $Re_\tau = 550$, (c,f) $Re_\tau = 950$.

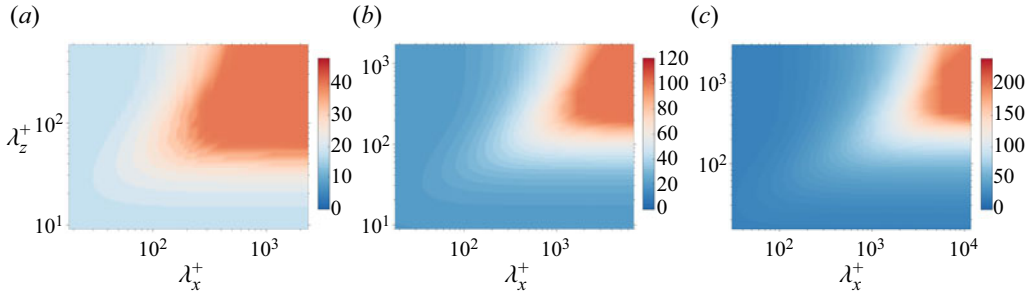


Figure 23. Distributions of the quasi-reference layer y_Q^+ at different wavelengths with $\omega = 10u_\tau/k_x$ in cases 180-40, 550-100 and 950-200.

where the expressions of \mathbf{R}_k and $\mathcal{C}(u, y^+)$ can be found in (2.7)–(2.8) and Appendix A, respectively.

Since the LCS calculated in (C2) is determined separately in each scale k , the height of the quasi-reference layer calculated from the LCS is also determined scale by scale. When the threshold LCS is 0.3 as adopted in this study, the value of y_Q^+ at the wavelength $(\lambda_x, \lambda_z) = (2\pi/k_x, 2\pi/k_z)$ with $\omega = 10u_\tau/k_x$ in cases 180-40, 550-100 and 950-200 are depicted in figure 23. It can be observed that the height of the quasi-reference layer tends to increase when the flow scale is larger.

In this study, we use the threshold LCS value (denoted as LCS_t) to determine the height of the quasi-reference layer, which has an important impact on the estimation result of the RWE. To efficiently modify the forcing profile, an ideal choice of the quasi-reference layer should be as high as possible under the premise of keeping the RBE valid for estimating the near-wall statistics. To test the impact of LCS_t on the estimation accuracy, the RWEs with five values of LCS_t equal to 0.1, 0.2, 0.3, 0.4 and 0.5 are set to estimate the streamwise

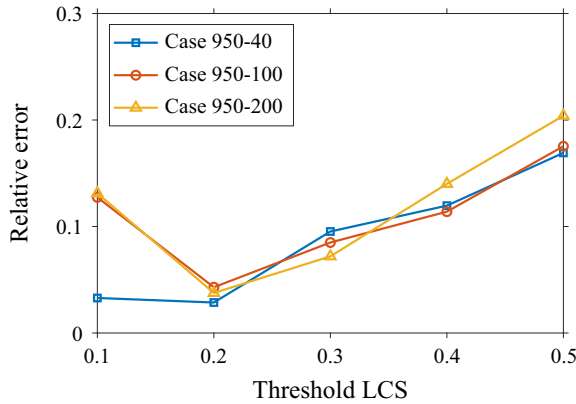


Figure 24. Impact of the threshold LCS on the estimation error of the streamwise r.m.s. profile.

Case	180-40	550-40	550-100	950-40	950-100	950-200
RWE	13.2	11.8	3.3	16.6	10.1	8.9
RBE	2.0	5.9	-28.0	7.7	-20.6	-47.4
λ -model	25.7	24.5	-8.5	17.5	-8.0	-24.0
WBE	109.7	122.1	113.4	103.6	115.2	115.7

Table 3. Summary of the relative percentage errors of the predicted streamwise r.m.s. velocity at the inner peak.

r.m.s. profiles in cases 950-40, 950-100 and 950-200. To quantify the relative estimation error in the tested cases, the integrated relative error of the streamwise r.m.s. profile is defined as

$$\epsilon = \left[\frac{\int_0^{y_R} (\mathbf{u}_{rms,RWE} - \mathbf{u}_{rms,DNS})^2 dy}{\int_0^{y_R} (\mathbf{u}_{rms,DNS})^2 dy} \right]^{0.5}. \quad (C3)$$

The estimation errors are summarized in [figure 24](#). A universal law between the relative error and LCS_t clearly exists in all the tested cases when $LCS_t \geq 0.2$. Although the tested cases with $LCS_t = 0.2$ appear to have the minimum errors, we notice that there are sharp increases of the relative error when LCS_t decreases from 0.2 to 0.1 in cases 950-100 and 950-200. Such increases in the estimation error are due to the underestimation of the fluctuation energy in the near-wall region when LCS_t is too low, in which case y_Q is too high so that the RBE becomes invalid to predict the near-wall statistics. To ensure the estimation accuracy in higher friction Reynolds numbers beyond 950, it is safer to conservatively set the value of LCS_t to be 0.3 to avoid the possible sharp increase of estimation error at $LCS_t = 0.2$. Thus, the threshold value of $LCS_t = 0.3$ is adopted as a default setting for all the cases with RWE in this study.

Appendix D. Relationship between the relative energy profiles of forcing and response

In this study, the relative forcing energy is modified between the wall and the quasi-reference layer y_Q , which is set to be unity upon y_Q then. The range of the relative

forcing energy to be modified is the same as the range of the target response estimated from RBE, both of which are below the quasi-reference layer. In the optimization problem of this study, the relationship between the forcing and response energy below the quasi-reference layer is expressed by

$$\hat{s}_k = \frac{\mathcal{R}_{k,1} \cdot \hat{w}_k + \mathcal{R}_{k,2} \cdot \hat{w}_1}{\mathcal{R}_{k,N_Q,1} \cdot \hat{w}_k + \mathcal{R}_{k,N_Q,2} \cdot \hat{w}_1}, \quad (D1)$$

where

$$\hat{s}_k = \frac{\text{diag}[\mathbf{S}_{u_i u_i, k}]_{y < y_Q}}{\text{diag}[\mathbf{S}_{u_i u_i, k}]_{y_Q}} \in \mathbb{C}^{N_Q-1} \quad (D2)$$

is the relative energy profile below the quasi-reference layer. The relative forcing energy profile $w_k(y)$ is split in (D1) as $w_k = [\hat{w}_k^T, \hat{w}_1^T]^T$, where $\hat{w}_k \in \mathbb{C}^{N_Q-1}$ is the relative forcing energy below y_Q that is to be determined, $\hat{w}_1 = [1, \dots, 1]_{N-N_Q+1}$ is that beyond y_Q . The linear operators in (D1) are expressed by $\mathcal{R}_{k,1} = \mathcal{C}_1 \mathcal{R}_k \mathcal{C}_1^T$, $\mathcal{R}_{k,2} = \mathcal{C}_1 \mathcal{R}_k \mathcal{C}_2^T$, $\mathcal{R}_{k,N_Q,1} = \mathcal{C}_{N_Q} \mathcal{R}_k \mathcal{C}_1^T$, $\mathcal{R}_{k,N_Q,2} = \mathcal{C}_{N_Q} \mathcal{R}_k \mathcal{C}_2^T$ and

$$\left. \begin{aligned} \mathcal{C}_1 &= \begin{bmatrix} \mathbf{I}_{(N_Q-1) \times (N_Q-1)} & \mathbf{O}_{(N_Q-1) \times (N-N_Q+1)} \end{bmatrix} \in \mathbb{C}^{(N_Q-1) \times N}, \\ \mathcal{C}_2 &= \begin{bmatrix} \mathbf{O}_{(N-N_Q+1) \times (N_Q-1)} & \mathbf{I}_{(N-N_Q+1) \times (N-N_Q+1)} \end{bmatrix} \in \mathbb{C}^{(N-N_Q+1) \times N}, \\ \mathcal{C}_{N_Q} &= \begin{bmatrix} \mathbf{O}_{1 \times (N_Q-1)} & 1 & \mathbf{O}_{1 \times (N-N_Q)} \end{bmatrix} \in \mathbb{C}^{1 \times N}, \\ \mathcal{R}_k &= \sum_{j=1}^3 \mathbf{R}_{k,i,j} \circ \overline{\mathbf{R}_{k,i,j}} \in \mathbb{C}^{N \times N}, \end{aligned} \right\} \quad (D3)$$

where $\mathbf{R}_{k,i,j}$ denotes the sub-matrix of the resolvent operator \mathbf{R}_k by selecting its rows for u_i and columns for the forcing in x_j direction, \circ denotes the element-wise matrix multiplication, and N_Q is the node number between y_Q and the wall.

REFERENCES

AMARAL, F.R., CAVALIERI, A.V.G., MARTINI, E., JORDAN, P. & TOWNE, A. 2021 Resolvent-based estimation of turbulent channel flow using wall measurements. *J. Fluid Mech.* **927**, A17.

BAARS, W.J., HUTCHINS, N. & MARUSIC, I. 2016 Spectral stochastic estimation of high-Reynolds-number wall-bounded turbulence for a refined inner-outer interaction model. *Phys. Rev. Fluids* **1** (5), 054406.

BAE, H.J., LOZANO-DURÁN, A., BOSE, S.T. & MOIN, P. 2018 Turbulence intensities in large-eddy simulation of wall-bounded flows. *Phys. Rev. Fluids* **3**, 014610.

BENEDDINE, S., SIPP, D., ARNAULT, A., DANDOIS, J. & LESSHAFFT, L. 2016 Conditions for validity of mean flow stability analysis. *J. Fluid Mech.* **798**, 485–504.

CESS, R.D. 1958 A survey of the literature on heat transfer in turbulent tube flow. *Tech. Rep.* 8-0529-R24. Westinghouse Research.

CHENG, C. & FU, L. 2022 Consistency between the attached-eddy model and the inner–outer interaction model: a study of streamwise wall-shear stress fluctuations in a turbulent channel flow. *J. Fluid Mech.* **942**, R9.

CHENG, C. & FU, L. 2023 A scale-based study of the Reynolds number scaling for the near-wall streamwise turbulence intensity in wall turbulence. *Intl J. Heat Fluid Flow* **101**, 109136.

CHENG, C., LI, W., LOZANO-DURÁN, A. & LIU, H. 2019 Identity of attached eddies in turbulent channel flows with bidimensional empirical mode decomposition. *J. Fluid Mech.* **870**, 1037–1071.

CHENG, C., SHYY, W. & FU, L. 2022 Streamwise inclination angle of wall-attached eddies in turbulent channel flows. *J. Fluid Mech.* **946**, A49.

CHEVALIER, M., HÖPFNER, J., BEWLEY, T.R. & HENNINGSON, D.S. 2006 State estimation in wall-bounded flow systems. Part 2. Turbulent flows. *J. Fluid Mech.* **552**, 167–187.

CHO, M., HWANG, Y. & CHOI, H. 2018 Scale interactions and spectral energy transfer in turbulent channel flow. *J. Fluid Mech.* **854**, 474–504.

- CHOI, H. & MOIN, P. 1990 On the space-time characteristics of wall-pressure fluctuations. *Phys. Fluids A: Fluid* **2** (8), 1450–1460.
- DEL ALAMO, J.C. & JIMÉNEZ, J. 2003 Spectra of the very large anisotropic scales in turbulent channels. *Phys. Fluids* **15** (6), L41–L44.
- FU, L., BOSE, S. & MOIN, P. 2022 Prediction of aerothermal characteristics of a generic hypersonic inlet flow. *Theor. Comput. Fluid Dyn.* **36** (2), 345–368.
- FU, L., KARP, M., BOSE, S.T., MOIN, P. & URZAY, J. 2021 Shock-induced heating and transition to turbulence in a hypersonic boundary layer. *J. Fluid Mech.* **909**, A8.
- FUKAGATA, K., IWAMOTO, K. & KASAGI, N. 2002 Contribution of Reynolds stress distribution to the skin friction in wall-bounded flows. *Phys. Fluids* **14** (11), L73–L76.
- GUASTONI, L., GÜEMES, A., IANIRO, A., DISCETTI, S., SCHLATTER, P., AZIZPOUR, H. & VINUESA, R. 2021 Convolutional-network models to predict wall-bounded turbulence from wall quantities. *J. Fluid Mech.* **928**, A27.
- GÜEMES, A., DISCETTI, S., IANIRO, A., SIRMACEK, B., AZIZPOUR, H. & VINUESA, R. 2021 From coarse wall measurements to turbulent velocity fields through deep learning. *Phys. Fluids* **33** (7), 075121.
- GUPTA, V., MADHUSUDANAN, A., WAN, M., ILLINGWORTH, S.J. & JUNIPER, M.P. 2021 Linear-model-based estimation in wall turbulence: improved stochastic forcing and eddy viscosity terms. *J. Fluid Mech.* **925**, A18.
- HE, G., JIN, G. & YANG, Y. 2017 Space-time correlations and dynamic coupling in turbulent flows. *Annu. Rev. Fluid Mech.* **49**, 51–70.
- HE, G.-W. & ZHANG, J.-B. 2006 Elliptic model for space-time correlations in turbulent shear flows. *Phys. Rev. E* **73** (5), 055303.
- HËPFFNER, J., CHEVALIER, M., BEWLEY, T.R. & HENNINGSON, D.S. 2005 State estimation in wall-bounded flow systems. Part 1. Perturbed laminar flows. *J. Fluid Mech.* **534**, 263–294.
- HOLFORD, J.J., LEE, M. & HWANG, Y. 2023 Optimal white-noise stochastic forcing for linear models of turbulent channel flow. *J. Fluid Mech.* **961**, A32.
- HOYAS, S. & JIMÉNEZ, J. 2008 Reynolds number effects on the Reynolds-stress budgets in turbulent channels. *Phys. Fluids* **20** (10), 101511.
- HWANG, Y. & COSSU, C. 2010 Linear non-normal energy amplification of harmonic and stochastic forcing in the turbulent channel flow. *J. Fluid Mech.* **664**, 51–73.
- ILLINGWORTH, S.J., MONTY, J.P. & MARUSIC, I. 2018 Estimating large-scale structures in wall turbulence using linear models. *J. Fluid Mech.* **842**, 146–162.
- JIMÉNEZ, J. 2018 Coherent structures in wall-bounded turbulence. *J. Fluid Mech.* **842**, P1.
- JOVANOVIĆ, M.R. & BAMIEH, B. 2005 Componentwise energy amplification in channel flows. *J. Fluid Mech.* **534**, 145–183.
- KARBAN, U., MARTINI, E., CAVALIERI, A.V.G., LESSHAFFT, L. & JORDAN, P. 2022 Self-similar mechanisms in wall turbulence studied using resolvent analysis. *J. Fluid Mech.* **939**, A36.
- KIM, J. & HUSSAIN, F. 1993 Propagation velocity of perturbations in turbulent channel flow. *Phys. Fluids A: Fluid* **5** (3), 695–706.
- KUNKEL, G.J. & MARUSIC, I. 2006 Study of the near-wall-turbulent region of the high-Reynolds-number boundary layer using an atmospheric flow. *J. Fluid Mech.* **548**, 375–402.
- LARSSON, J., KAWAI, S., BODART, J. & BERMEJO-MORENO, I. 2016 Large eddy simulation with modeled wall-stress: recent progress and future directions. *Mech. Engng Rev.* **3** (1), 15–00418.
- LEE, J.H. & SUNG, H.J. 2013 Comparison of very-large-scale motions of turbulent pipe and boundary layer simulations. *Phys. Fluids* **25** (4), 045103.
- LUHAR, M., SHARMA, A.S. & MCKEON, B.J. 2015 A framework for studying the effect of compliant surfaces on wall turbulence. *J. Fluid Mech.* **768**, 415–441.
- MADHUSUDANAN, A., ILLINGWORTH, S.J. & MARUSIC, I. 2019 Coherent large-scale structures from the linearized Navier–Stokes equations. *J. Fluid Mech.* **873**, 89–109.
- MARTINI, E., CAVALIERI, A.V.G., JORDAN, P., TOWNE, A. & LESSHAFFT, L. 2020 Resolvent-based optimal estimation of transitional and turbulent flows. *J. Fluid Mech.* **900**, A2.
- MARUSIC, I. & HEUER, W.D.C. 2007 Reynolds number invariance of the structure inclination angle in wall turbulence. *Phys. Rev. Lett.* **99** (11), 114504.
- MARUSIC, I., MATHIS, R. & HUTCHINS, N. 2010 Predictive model for wall-bounded turbulent flow. *Science* **329** (5988), 193–196.
- MCKEON, B.J. 2017 The engine behind (wall) turbulence: perspectives on scale interactions. *J. Fluid Mech.* **817**, P1.
- MCKEON, B.J. & SHARMA, A.S. 2010 A critical-layer framework for turbulent pipe flow. *J. Fluid Mech.* **658**, 336–382.

- MENEVEAU, C. & MARUSIC, I. 2013 Generalized logarithmic law for high-order moments in turbulent boundary layers. *J. Fluid Mech.* **719**, R1.
- MOARREF, R., SHARMA, A.S., TROPP, J.A. & MCKEON, B.J. 2013 Model-based scaling of the streamwise energy density in high-Reynolds-number turbulent channels. *J. Fluid Mech.* **734**, 275–316.
- MOMOH, J.A., EL-HAWARY, M.E. & ADAPA, R. 1999 A review of selected optimal power flow literature to 1993. II. Newton, linear programming and interior point methods. *IEEE Trans. Power Syst.* **14** (1), 105–111.
- MONTY, J.P., HUTCHINS, N., NG, H.C.H., MARUSIC, I. & CHONG, M.S. 2009 A comparison of turbulent pipe, channel and boundary layer flows. *J. Fluid Mech.* **632**, 431–442.
- MORRA, P., NOGUEIRA, P.A.S., CAVALIERI, A.V.G. & HENNINGSON, D.S. 2021 The colour of forcing statistics in resolvent analyses of turbulent channel flows. *J. Fluid Mech.* **907**, A24.
- MORRA, P., SEMERARO, O., HENNINGSON, D.S. & COSSU, C. 2019 On the relevance of Reynolds stresses in resolvent analyses of turbulent wall-bounded flows. *J. Fluid Mech.* **867**, 969–984.
- NAKASHIMA, S., FUKAGATA, K. & LUHAR, M. 2017 Assessment of suboptimal control for turbulent skin friction reduction via resolvent analysis. *J. Fluid Mech.* **828**, 496–526.
- PICKERING, E., RIGAS, G., SCHMIDT, O.T., SIPP, D. & COLONIUS, T. 2021 Optimal eddy viscosity for resolvent-based models of coherent structures in turbulent jets. *J. Fluid Mech.* **917**, A29.
- REYNOLDS, W.C. & HUSSAIN, A.K.M.F. 1972 The mechanics of an organized wave in turbulent shear flow. Part 3. Theoretical models and comparisons with experiments. *J. Fluid Mech.* **54** (2), 263–288.
- SCHMIDT, O.T., TOWNE, A., RIGAS, G., COLONIUS, T. & BRÈS, G.A. 2018 Spectral analysis of jet turbulence. *J. Fluid Mech.* **855**, 953–982.
- SHARMA, A.S. & MCKEON, B.J. 2013 On coherent structure in wall turbulence. *J. Fluid Mech.* **728**, 196–238.
- DE SILVA, C.M., MARUSIC, I., WOODCOCK, J.D. & MENEVEAU, C. 2015 Scaling of second- and higher-order structure functions in turbulent boundary layers. *J. Fluid Mech.* **769**, 654–686.
- SMITS, A.J., MCKEON, B.J. & MARUSIC, I. 2011 High-Reynolds number wall turbulence. *Annu. Rev. Fluid Mech.* **43**, 353–375.
- TAYLOR, G.I. 1938 The spectrum of turbulence. *Proc. R. Soc. Lond. A* **164** (919), 476–490.
- TOWNE, A., LOZANO-DURÁN, A. & YANG, X. 2020 Resolvent-based estimation of space–time flow statistics. *J. Fluid Mech.* **883**, A17.
- TOWNE, A., SCHMIDT, O.T. & COLONIUS, T. 2018 Spectral proper orthogonal decomposition and its relationship to dynamic mode decomposition and resolvent analysis. *J. Fluid Mech.* **847**, 821–867.
- TOWNSEND, A.A. 1976 *The Structure of Turbulent Shear Flow*, 2nd edn. Cambridge University Press.
- YANG, B., JIN, G., WU, T., YANG, Z. & HE, G. 2020 Numerical implementation and evaluation of resolvent-based estimation for space–time energy spectra in turbulent channel flows. *Acta Mechanica Sin.* **36**, 775–788.
- YANG, X.I.A., MARUSIC, I. & MENEVEAU, C. 2016 Hierarchical random additive process and logarithmic scaling of generalized high order, two-point correlations in turbulent boundary layer flow. *Phys. Rev. Fluids* **1** (2), 024402.